Univerzita Karlova v Praze
Matematicko-fyzikální fakulta

DIPLOMOVÁ PRÁCE

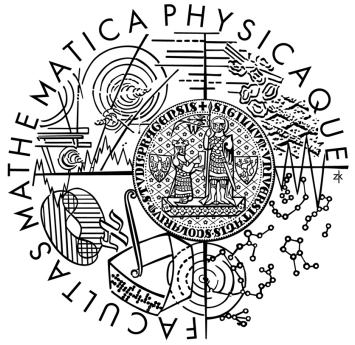

Bc. Petr Opletal

Kritické chování v magnetických fázových diagramech uranových sloučenin

Katedra fyziky kondenzovaných látek

Vedoucí diplomové práce: RNDr. Jan Prokleška, Ph.D.

Studijní program: Fyzika
Studijní obor: Fyzika kondenzovaných soustav a materiálů

Praha 2015

Charles University in Prague
Faculty of Mathematics and Physics

MASTER THESIS

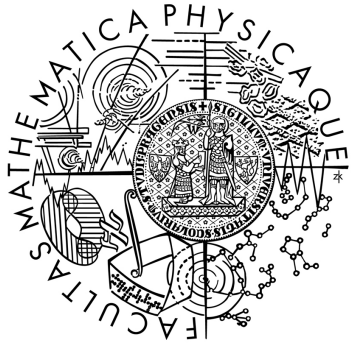

Bc. Petr Opletal

Critical behavior in magnetic phase diagrams of uranium compounds

Department of Condensed Matter Physics

Supervisor of the master thesis: RNDr. Jan Prokleška, Ph.D.

Study programme: Physics
Specialization: Physics of Condensed Matter and Materials

Prague 2015

I would like to thank my supervisor RNDr. Jan Prokleška Ph.D. for his helpful support, time and advices in my work and patience with me. I would also like to thank to prof. RNDr. Vladimír Sechovský, DrSc. for his comments and suggestions. I also thank to RNDr. Michal Vališka and Ing. Barbora Vondráčková for their help and advises in laboratories. I want to thank to RNDr. Jan Valenta for his help with preparing hydrostatic pressure measurements. Last but not least I want to thank to my family and my girlfriend for all their support.

I declare that I carried out this master thesis independently, and only with the cited sources, literature and other professional sources.

I understand that my work relates to the rights and obligations under the Act No. 121/2000 Coll., the Copyright Act, as amended, in particular the fact that the Charles University in Prague has the right to conclude a license agreement on the use of this work as a school work pursuant to Section 60 paragraph 1 of the Copyright Act.

In Prague date ..... Bc. Petr Opletal

Název práce: Kritické chování v magnetických fázových diagramech uranových sloučenin

Autor: Bc. Petr Opletal

Katedra: Katedra fyziky kondenzovaných látek

Vedoucí diplomové práce: RNDr. Jan Prokleška, Ph.D., Katedra fyziky kondenzovaných látek

Abstrakt: Tato práce se zabývá studiem fázových diagramů a kritických jevů s nimi spojených v pseudoternárních sloučeninách $UCo_{1-x}Ru_xAl$. Tři monokrystaly o nominálním složení $UCo_{0,99}Ru_{0,01}Al$, $UCo_{0,995}Ru_{0,005}Al$ a $UCo_{0,9975}Ru_{0,0025}Al$ byli připraveny Czochralskeho metodou. Jejich kvalita byla ověřena EDX analýzou, Laueho metodou a rentgenovou práškovou difrakcí. Pro $UCo_{0,99}Ru_{0,01}Al$ byla určena Curieova teplota $T_C = 16$ K. $UCo_{0,995}Ru_{0,005}Al$ má přechod z paramagnetické do feromagnetické fáze v $T_C = 4{,}5$ K a ve vyšších teplotách se objevuje metamagneticky přechod prvního druhu s kritickým polem $H_C = 0{,}04$ T. $UCo_{0,9975}Ru_{0,0025}Al$ je paramagnetické do nejnižších teplot s metamagnetickým přechodem prvního druhu s kritickým polem $H_C = 0{,}55$ T. Hydrostatické tlakové experimenty na $UCo_{0,995}Ru_{0,005}Al$ a $UCo_{0,9975}Ru_{0,0025}Al$ ukázali, že feromagnetismus zanikne a kritické pole se zvyšuje s rostoucím tlakem. Toto chování připomíná vývoj magnetismu v UCoAl a URhAl pod vlivem hydrostatického tlaku.

Klíčová slova: UCoAl, URuAl, feromagnetismus, metamagnetismus

Title: Critical behavior in magnetic phase diagrams of uranium compounds

Author: Bc. Petr Opletal

Department: Department of Condensed Matter Physics

Supervisor: RNDr. Jan Prokleška, Ph.D., Department of Condensed Matter Physics

Abstract: This work is focused on study of phase diagrams and related critical effects in the pseudoternary $UCo_{1-x}Ru_xAl$ compound. Three single crystals of nominal composition $UCo_{0.99}Ru_{0.01}Al$, $UCo_{0.995}Ru_{0.005}Al$ and $UCo_{0.9975}Ru_{0.0025}Al$ have been prepared by Czochralski method in triarc furnace. Quality of single crystals was checked by EDX analysis, Laue method and XRPD. For $UCo_{0.99}Ru_{0.01}Al$ Curie temperature was determined as $T_C = 16$ K. $UCo_{0.995}Ru_{0.005}Al$ shows transition from paramagnetic to ferromagnetic phase at $T_C = 4.5$ K and at higher temperatures we observe a metamagnetic transition of first order with a critical field $H_C = 0.04$ T. $UCo_{0.9975}Ru_{0.0025}Al$ is paramagnetic to low temperatures with metamagnetic transition of first order and critical field $H_C = 0.55$ T. Experiments in hydrostatic pressure on $UCo_{0.995}Ru_{0.005}Al$ and $UCo_{0.9975}Ru_{0.0025}Al$ showed decay of ferromagnetism and increase of critical field. This behavior is similar to evolution of magnetism in UCoAl and URhAl in applied hydrostatic pressure.

Keywords: UCoAl, URuAl, ferromagnetism, metamagnetism

Contents

1 Introduction **3**
- 1.1 Motivation of the thesis . . . 3
- 1.2 Outline of the thesis . . . 4

2 Theory **5**
- 2.1 Magnetism . . . 5
  - 2.1.1 An atom/ion in magnetic field . . . 5
  - 2.1.2 Diamagnetism . . . 6
  - 2.1.3 Paramagnetism . . . 7
  - 2.1.4 Magnetic interactions . . . 7
  - 2.1.5 Magnetic ordering . . . 9
  - 2.1.6 Magnetism in *3d*, *4f* and *5f* ions and their intermetallics . . . 10
- 2.2 Quantum phase transitions and quantum critical point . . . 13
- 2.3 Electrical resistance . . . 15

3 Physics of UCoAl **16**

4 Experimental methods **19**
- 4.1 Sample preparations . . . 19
  - 4.1.1 Czochralski method . . . 19
  - 4.1.2 Sample annealing . . . 19
- 4.2 Sample characterization methods . . . 19
  - 4.2.1 X-ray methods . . . 20
  - 4.2.2 EDX . . . 21
- 4.3 MPMS . . . 21
- 4.4 PPMS . . . 22
  - 4.4.1 Electric properties measurements . . . 22
- 4.5 Pressure cells . . . 23

5 Results **24**
- 5.1 Samples preparation . . . 24
- 5.2 Single crystals characterization . . . 24
  - 5.2.1 Laue method . . . 24
  - 5.2.2 EDX analysis . . . 25
  - 5.2.3 Results of XRPD . . . 25
  - 5.2.4 Analysis by magnetic measurements . . . 26
- 5.3 $UCo_{0.99}Ru_{0.01}Al$ single crystal study . . . 26
  - 5.3.1 Magnetization measurements . . . 26
- 5.4 $UCo_{0.995}Ru_{0.005}Al$ single crystal study . . . 27
  - 5.4.1 Magnetization measurements . . . 27
  - 5.4.2 Electric resistivity measurements . . . 29
- 5.5 $UCo_{0.9975}Ru_{0.0025}Al$ single crystal study . . . 30
  - 5.5.1 Magnetization measurements . . . 30
  - 5.5.2 Electric resistivity measurements . . . 30
- 5.6 Magnetization measurements in hydrostatic pressure . . . 32

5.6.1 $UCo_{0.995}Ru_{0.005}Al$ 32
5.6.2 $UCo_{0.9975}Ru_{0.0025}Al$ 32

6 General discussion **36**

7 Conclusions and future plans **39**

References **40**

List of Tables **43**

1. Introduction

Phase transitions and related critical behavior are always intensively studied by theoretical and also experimental physicists. In recent years new interesting phenomena were discovered, where phase transition is in absolute zero temperature, called quantum phase transition. Rare-earth intermetallics based mainly on Ce and Yb, which mostly order antiferromagnetically, were main focus because of their unstable $4f$ electron states. In these compounds coexistence of antiferromagnetic ordering and superconductivity, heavy fermions and other interesting properties were observed. This led to large interest in their phase diagrams with antiferromagnetic phase.

Not only intermetallics with rare-earth elements show interesting properties. Actinide intermetallics and mainly uranium intermetallics exhibited similar properties as rare-earth intermetallics, which can be tuned by various parameters. The $5f$ electron states of uranium are not localized as $4f$ electronic states and interact with electron of neighboring ions, meaning they are on border of localized and itinerant character. Their character can be easily tuned by external pressure, chemical doping and magnetic field.

In recent years, new type of quantum criticality in ferromagnets was described by the generalized phase diagram (Figure 1.1). In this phase diagram many interesting critical points are observed. Due to difficulty of getting high quality samples or reaching high pressures, there are not many compounds with phase diagram similar to the generalized one and it is hard to study these critical points. Uranium intermetallics are good candidates, because of their easy tuneability and low Curie temperatures in general. One of the compounds with phase diagram similar to generalized one is UCoAl. It crystallizes in the hexagonal ZrNiAl-type structure and it is a paramagnet down to low temperatures with metamagnetic transition of the first order in the critical field of $\sim$ 0.7 T up to 11 K [1]. With applying hydrostatic pressure metamagnetic transition is suppressed and a quantum critical endpoint is reached, similarly to the generalized phase diagram.

1.1 Motivation of the thesis

Motivation of my thesis is to study phase diagram of UCoAl doped by Ru on Co positions. It was shown that already 1% of ruthenium induces ferromagnetism [3]. By substituting cobalt ions with ruthenium, we reach a ferromagnetic phase in B-T phase diagram, which is situated in a negative pressure for pure UCoAl. If we apply hydrostatic pressure, we can expect to reach similar state as UCoAl in ambient pressure and achieve all critical points of the generalized phase diagram.

In my thesis we investigate the magnetic phase diagrams of $UCo_{1-x}Ru_xAl$ compounds for nominal values x=0.01, $x = 0.005$ and $x = 0.0025$ by measuring magnetic and electric transport properties in ambient and hydrostatic pressure. We expect to find the critical points, construct phase diagrams and discuss results in terms of the generalized phase diagram.

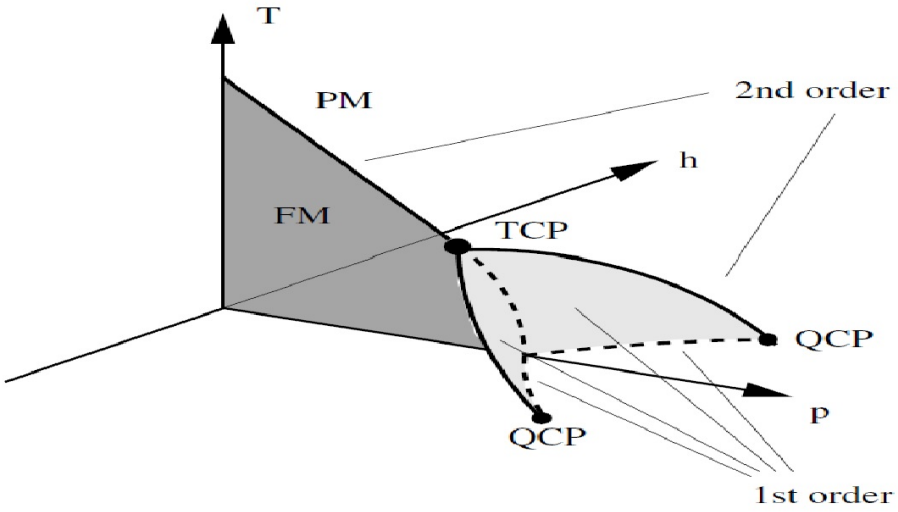

Figure 1.1: Generalized phase diagram for ferromagnets. p is tuning parameter(hydrosttic pressure, chemical doping) and h is magnetic field [2].

1.2 Outline of the thesis

This work has seven chapters including this Introduction. Second part is brief theoretical overview of topics and terms used in this thesis. Next part includes description of UCoAl and its phase diagram. Fourth part focuses on overview of experimental methods used. Results are summarized in chapter 5 individually for each crystal. General discussion of results is in Chapter 6. Final conclusions and future plans are summarized in Chapter 7.

2. Theory

2.1 Magnetism

Solids consist of very large number of atoms with their own magnetic moment. Magnetic moment is defined as:

$$\mu = IS \tag{2.1}$$

where I is electric current going through loop of the area S and direction of magnetic moment μ is normal to the area of current loop. To summarize all magnetic moments μ of atoms and ions in solid we define magnetization $\boldsymbol{M}$ as magnetic moment per unit volume. $\boldsymbol{M}$ is considered to be a vector field inside the solid. In special cases where relation between magnetization $\boldsymbol{M}$ and magnetic field $\boldsymbol{H}$ is linear we get

$$\boldsymbol{H} = \chi \boldsymbol{M}. \tag{2.2}$$

The solid in this situation is called linear material. χ is called magnetic susceptibility. Relation between magnetic induction $\boldsymbol{B}$ and $\boldsymbol{M}$ in the linear material is given by

$$\boldsymbol{B} = \mu_0 \left(\boldsymbol{M} + \chi \boldsymbol{M}\right) = \mu_0 \left(1 + \chi\right) \boldsymbol{M} = \mu_0 \mu_\mathrm{r} \boldsymbol{M} \tag{2.3}$$

where μ_0 is the permeability of vacuum and μ_r is the permeability of the material.

For magnetic moments of atoms/ions, we can think of electric current I as a electron of mass m and electric charge $-e$ orbiting around atomic core. For that we use the mass of electron m_e and charge $-e$. This could be then interpreted as

$$I = \frac{-e}{T} = \frac{-ev}{2\pi r} \tag{2.4}$$

where T is the orbital period, v is the velocity and r is the radius of the orbit. From quantum mechanics [4], we know that the angular momentum of electron ground state is

$$m_\mathrm{e} v r = \hbar. \tag{2.5}$$

Using equations (2.1), (2.4) and (2.5) we get

$$\mu = \pi r^2 I = -\frac{evr}{2} = -\frac{-e\hbar}{2m_\mathrm{e}} = -\mu_\mathrm{B} \quad ; \qquad \mu_\mathrm{B} = -\frac{e\hbar}{2m_\mathrm{e}} \tag{2.6}$$

where μ_B is the Bohr magneton and is used as unit of magnetic moments on atomic scale.

2.1.1 An atom/ion in magnetic field

Each electron orbiting in atom/ion has the spin angular moment $\boldsymbol{S}$ and the orbital angular moment $\boldsymbol{L}$ [4]. The total orbital angular moment $\boldsymbol{L}$ of all electrons in an atom/ion is

$$\hbar \boldsymbol{L} = \sum_{i=1}^{Z} \boldsymbol{r_\mathrm{i}} \times \boldsymbol{p_\mathrm{i}} \tag{2.7}$$

and total spin angular moment of atom/ion will be

$$\boldsymbol{S} = \sum_{i=1}^{Z} \boldsymbol{S_i} \tag{2.8}$$

where Z is total number of electrons in the atom/ion, $\boldsymbol{r_i}$ is the position of the i^{th} electron, $\boldsymbol{p_i}$ is its momentum and $\boldsymbol{S_i}$ is its spin angular moment. For an electron in a free atom/ion we get Hamiltonian [4]

$$\widehat{\boldsymbol{H}_0} = \sum_{i=1}^{Z} \left(\frac{p_i^2}{2m_e} + V_i \right) \tag{2.9}$$

where $\frac{p_i^2}{2m_e}$ is the kinetic energy of the i^{th} electron and V_i is the potential energy of the i^{th} electron. Placing atom/ion into the magnetic field of induction $\boldsymbol{B}$ changes the Hamiltonian and the new Hamiltonian will be [4]

$$\widehat{\boldsymbol{H}} = \widehat{\boldsymbol{H}_0} + \mu_B \left(\boldsymbol{L} + g\boldsymbol{S} \right) \boldsymbol{B} + \frac{e^2}{8m_e} \sum_{i=1}^{Z} \left(\boldsymbol{B} \times \boldsymbol{r_i} \right)^2 \tag{2.10}$$

where g is the g-factor. The term $\mu_B \left(\boldsymbol{L} + g\boldsymbol{S} \right) \boldsymbol{B}$ represents the atom's/ion's own magnetic moment and is called paramagnetic. The term $\frac{e^2}{8m_e} \sum_{i=1}^{Z} \left(\boldsymbol{B} \times \boldsymbol{r_i} \right)^2$ is known as diamagnetic moment. We can find two responses of matter on applied external magnetic field, depending on which term is prominent. We distinguish diamagnetic (diamagnetism) and paramagnetic (paramagnetism) response.

2.1.2 Diamagnetism

Diamagnetic substances have a negative magnetic susceptibility. If we apply an external magnetic field then a magnetic moment in opposite direction is induced. Ignoring the paramagnetic term in equation (2.10), for example because of zero $\boldsymbol{S}$ and $\boldsymbol{L}$ and $\mathbf{B}$ parallel to z axis. We can then write

$$\left(\boldsymbol{B} \times \boldsymbol{r}_i \right)^2 = \boldsymbol{B}^2 \left(x_i^2 + y_i^2 \right). \tag{2.11}$$

First-order energy shift in the ground state energy will be

$$\Delta E_0 = \frac{e^2 B^2}{8m_e} \sum_{i=1}^{Z} \left\langle 0 \mid x_i^2 + y_i^2 \mid 0 \right\rangle \tag{2.12}$$

where $\mid 0\rangle$ is the ground state wave function. For spherically symmetric atom we can write $\langle x_i^2 \rangle = \langle y_i^2 \rangle = \frac{1}{3} \langle r_i^2 \rangle$ and 2.12 can be written as

$$\Delta E_0 = \frac{e^2 B^2}{8m_e} \sum_{i=1}^{Z} \left\langle 0 \mid r_i^2 \mid 0 \right\rangle. \tag{2.13}$$

Considering solid composed of N ions (each with Z electrons of mass m_e) with all shells filled in volume V. Magnetization (at $T = 0$ K) can be derived as

$$M = -\frac{\partial F}{\partial B} = -\frac{N}{V} \frac{\partial \Delta E_0}{\partial B} = -\frac{Ne^2 B}{6m_e} \sum_{i=1}^{Z} \left\langle 0 \mid r_i^2 \mid 0 \right\rangle \tag{2.14}$$

where F is Helmholtz free energy. Diamagnetic susceptibility can be extracted as $\chi = M/H \cong \mu_0 M/B$ and we get diamagnetic susceptibility defined as

$$\chi = -\frac{Ne^2\mu_0}{6Vm_\mathrm{e}} \sum_{i=1}^{Z} \langle r_\mathrm{i}^2 \rangle. \tag{2.15}$$

From equation (2.15) one can see that the susceptibility is negative and temperature independent.

2.1.3 Paramagnetism

If the first term in equation (2.10) is dominant, than substance behaves as paramagnet. By applying external magnetic field on paramagnetic substance, magnetic moment parallel with external field is induced. By ignoring quantification of magnetic moment and that it can point only in certain directions (semiclassical treatment of paramagnetism), we get temperature T dependent paramagnetic susceptibility in form

$$\chi = \frac{n\mu_0\mu_\mathrm{eff}}{3k_\mathrm{B}T} = \frac{C}{T} \tag{2.16}$$

where n is the number of magnetic moments per unit volume, μ_eff is the effective magnetic moment and k_B is Boltzmann constant. The equation (2.16) is known as Curie's law (C is Curie constant characteristic for every material) and shows that the magnetic susceptibility is positive, inversely proportional to temperature and independent on the external applied magnetic field.

It is also important to note that most of paramagnetic ions contain closed inner shells, which responds to magnetic field diamagnetically, but the paramagnetic term is several orders larger than the diamagnetic one.

2.1.4 Magnetic interactions

Collective ordering of magnetic moments in solid cannot be explained by theory above. To explain this long range correlations between magnetic moments we must think of magnetic interactions between magnetic moments. The most simple model considers the interaction between two electrons. From this model we obtain simple exchange Hamiltonian [4]

$$\widehat{\boldsymbol{H}}_{ex} = -2J\boldsymbol{S_1}\boldsymbol{S_2} \tag{2.17}$$

where $\boldsymbol{S_1}$ and $\boldsymbol{S_2}$ are appropriate quantum numbers and J is exchange constant or exchange integral. For positive (negative) value of J magnetic moments will be parallel (antiparallel).

Phenomena of exchange interactions is important for the long range magnetic ordering. This effect is purely quantum mechanical. Model for two electrons can be generalized to a many-body system. Most studied model for many-body system is Heisenberg model, which considers interaction between nearest neighbors. The Hamiltonian introduced by the Heisenberg model

$$\widehat{\mathbf{H}}_{Heis} = -\sum_{\langle i,j \rangle} J_\mathrm{ij}\boldsymbol{S}_\mathbf{i}\boldsymbol{S}_\mathbf{j} \tag{2.18}$$

where J is nonzero only for nearest neighbors.
Direct exchange: If wavefunctions of electrons responsible for magnetic ordering directly overlap than we talk about direct interaction. Exchange integral for this interaction reaches values around 10^2 - 10^3 K and it is realized in *3d*, *4d*, *5d* and *5f* atoms/ions. Direct exchange is interaction without any intermediary and only between neighboring atoms therefore it can be classified as short range interaction (Figure 2.1).

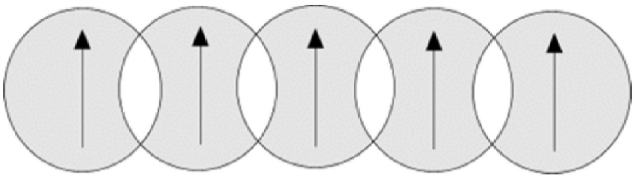

Figure 2.1: Schematic of the direct exchange interaction. Arrows represent magnetic moments [5].

Indirect exchange: The indirect exchange interaction (superexchange) is interaction between the non-neighboring magnetic ions mediated by a non-magnetic ion (usually p or d element) sitting between the magnetic ions (Figure 2.2). Exchange integral has value around 10^0 – 10^2 K. This kind of interaction can be found in compounds with *3d*, *4d*, *5d*, *4f* and *5f* compounds.

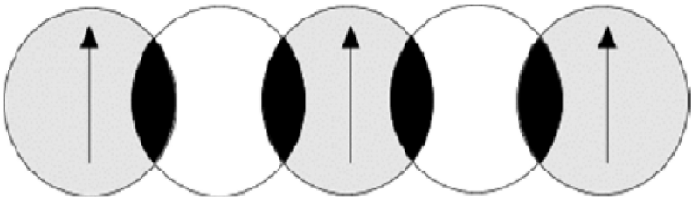

Figure 2.2: Schematic of the indirect exchange interaction. Arrows represent magnetic moments [5].

RKKY: In rare earth metals and their compounds we can find special sort of indirect exchange interaction called RKKY (after Ruderman, Kittel, Kasuya and Yosida) [6, 7, 8]. Interactions is mediated by conduction electrons which interact with localized $4f$ electrons (Figure 2.3). $4f$ electrons cannot interact directly or indirectly because of their localization. For large $\boldsymbol{r}$ the interaction can be described by

$$J_{\mathrm{RKKY}} \propto \frac{\cos\left(2k_{\mathrm{F}}r\right)}{r^3} \tag{2.19}$$

where k_{F} is Fermi surface radius and thanks to the cos function, the type of magnetic ordering depends on distance of ions. Values of exchange integral can reach 10^0 – 10^2 K.

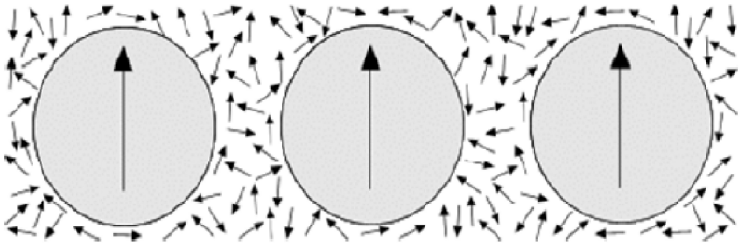

Figure 2.3: Schematic of the RKKY exchange interaction. Arrows represent magnetic moments [5].

2.1.5 Magnetic ordering

Lowering temperature we reach point, where energy of thermal fluctuations is smaller than energy of exchange interaction and spontaneous magnetic ordering occurs. This is called critical temperature. Depending on sign of exchange integral and value of magnetic moments we observe different long-range magnetic structures.

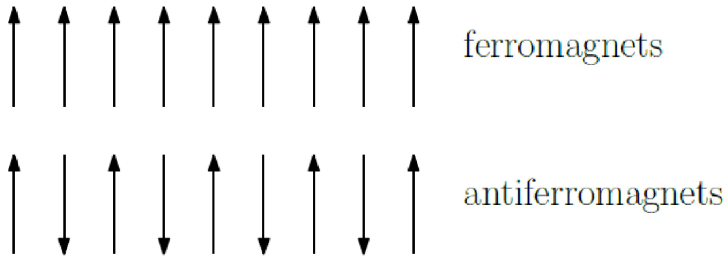

Figure 2.4: The basic types of magnetic ordering. Arrows represent magnetic moments [5].

Ferromagnetism : In a simple ferromagnet all magnetic moments align in one unique direction (Figure 2.4). Spontaneous magnetic ordering appears below the Curie temperature T_{C}. Behavior of simple ferromagnet can be described Weiss model, where we approximate exchange interaction by effective magnetic field $\boldsymbol{B}_{\mathrm{mf}}$ [4] inside solid. Further, we assume that molecular field is linearly dependent on magnetization

$$\boldsymbol{B}_{\mathrm{mf}} = \lambda \boldsymbol{M} \tag{2.20}$$

where λ is a constant which parametrizes the strength of the molecular magnetic field, it is temperature independent and positive for ferromagnets. The problem can be now treated as paramagnet placed in magnetic field $\boldsymbol{B} + \boldsymbol{B}_{\mathrm{mf}}$. The paramagnetic susceptibility will be

$$\chi_{\mathrm{P}} = \frac{\mu_0 M}{(\boldsymbol{B} + \boldsymbol{B}_{\mathrm{eff}})} = \frac{C}{T} \tag{2.21}$$

where C is Curie constant. If we substitute (2.20) in (2.21) we obtain

$$\chi = \frac{M}{\mu_0 B} = \frac{C}{T - C\lambda} \tag{2.22}$$

. For $T = C\lambda = T_{\mathrm{C}}$, susceptibility has singularity. At this temperature a spontaneous magnetization emerges. From (2.22) we get Curie-Weiss law

$$\chi = \frac{C}{T - \Theta_{\mathrm{P}}} \tag{2.23}$$

where Θ_{P} is paramagnetic Curie temperature, which is connected to strength of exchange interaction. In Figure 2.1.5 we can see typical dependence of magnetization and susceptibility on temperature for ferromagnets.

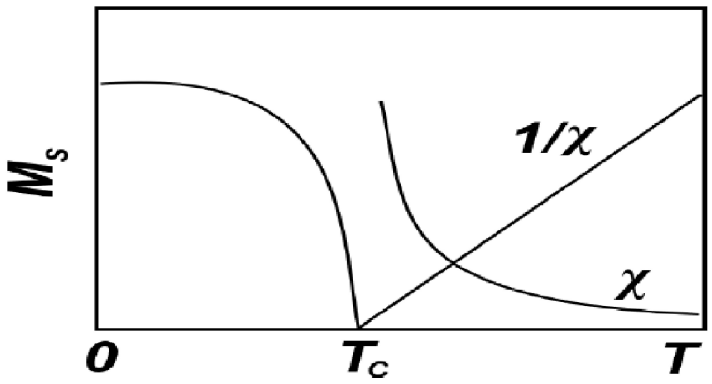

Figure 2.5: Temperature dependence of susceptibility χ, inverse susceptibility $1/\chi$ and the spontaneous magnetization of a ferromagnetM_{S}.

Antiferromagnetism: In a simple antiferromagnet adjacent magnetic moments are oriented antiparallely and the exchange integral J has negative sign (Figure 2.4). In antiferromagnets, critical temperature at which the magnetic moments order is called Néel temperature T_{N}. The simple antiferromagnet can be described as system composed of two interpenetrating sublatices, where the magnetic moments of one sublattice points up and the other ones point down. The magnetic susceptibility at temperatures above T_{N} follows also Curie-Weiss law. In general we can say that Curie-Weiss law

$$\chi = \chi_0 + \frac{C}{T - \Theta_{\mathrm{P}}} \tag{2.24}$$

represents behaviour of paramagnets, ferromagnets and antiferromagnets. For simple paramagnet Θ_{P} is zero, whereas Θ_{P} of a simple ferromagnet (antiferromagnet) is positive (negative). The paramagnetic Curie temperatures of real systems are often different from theory and therefore it needs to be treated individually.

2.1.6 Magnetism in *3d*, *4f* and *5f* ions and their intermetallics

***3d* magnetism – band ferromagnetism (itinerant ferromagnetism)**: In band ferromagnetism electrons near Fermi energy E_{F} from spin-down band

with energy $E_{\mathrm{F}} - \delta E$ are taken to E_{F} and their spin is flipped and placed in spin-up band where they sit with energies from E_{F} to $E_{\mathrm{F}} + \delta E$. The number of electrons moved can be expressed as $g\left(E_{\mathrm{F}}\right)\delta E/2$ and increase in energy δE. The total change in energy is $g\left(E_{\mathrm{F}}\right)\delta E/2 \times \delta E$. The total change of kinetic energy ΔE_{KE} is

$$\Delta E_{\mathrm{KE}} = \frac{1}{2} g\left(E_{\mathrm{F}}\right)\left(\delta E\right)^2 . \tag{2.25}$$

The energy cost in form of kinetic energy is compensated by energy of interaction of magnetization with molecular field. The density of up-spins is $n_{\mathrm{u}} = \frac{1}{2}\left(n + g\left(E_{\mathrm{F}}\right)\delta E\right)$ and density of down-spins is $n_{\mathrm{d}} = \frac{1}{2}\left(n - g\left(E_{\mathrm{F}}\right)\delta E\right)$. Therefore magnetization is $M = \mu_{\mathrm{B}}\left(n_{\mathrm{u}} - n_{\mathrm{d}}\right)$, if we assume each electron has magnetic moment of 1 μ_{B}. The energy of molecular field is [4]

$$\begin{aligned} \Delta E_{\mathrm{PE}} = & -\int_0^M \mu_0 \lambda M' dM' = -\frac{1}{2}\mu_0 \lambda M^2 = \\ & -\frac{1}{2}\mu_0 \mu_{\mathrm{B}}^2 \lambda \left(n_{\mathrm{u}} - n_{\mathrm{d}}\right)^2 = -\frac{1}{2} U \left(g\left(E_{\mathrm{F}}\right)\delta E\right)^2 \end{aligned} \tag{2.26}$$

where $U = \mu_0 \mu_{\mathrm{B}}^2 \lambda$ is measure of Coulomb energy which corresponds to molecular field which is due exchange interaction which is due coulomb interaction. The total change of energy is

$$\Delta E = \Delta E_{\mathrm{KE}} + \Delta E_{\mathrm{PE}} = \frac{1}{2} g\left(E_{\mathrm{F}}\right)\left(\delta E\right)^2 \left(1 - U g\left(E_{\mathrm{F}}\right)\right). \tag{2.27}$$

The magnetic moments spontaneously align if $\Delta E < 0$, which implies

$$U g\left(E_{\mathrm{F}}\right) \geq 1. \tag{2.28}$$

This is known as Stoner criterion [4]. Large density near Fermi energy and strong Coulomb effects are required for ferromagnetic instability.

***4f* magnetism - localized magnetism**: Majority of *4f* electron density is lies deeply inside the core of a lanthanide atoms. This leads to weak interaction with environment. This fact is documented thanks to neutron spectroscopy experiments [9] which have revealed negligible mixing of *4f* states of majority of lanthanides with conduction and valence electron states of neighbouring atoms. In band magnetism the angular moment $\boldsymbol{L}$ is very small thanks to the delocalization of *3d* states, and thus only spin is considered. In *4f* magnetism, because of localization of states we must consider angular moment and spin. Rare earth metal atoms are heavy and we must therefore take in account spin-orbit coupling and introduce total angular momentum $\boldsymbol{J}$, defined as $\boldsymbol{J} = \boldsymbol{L} + \boldsymbol{S}$ [4]. Observed ground magnetic states agree well with the corresponding RE^{3+} free ion values calculated within spin-orbit coupling scheme for most $4f$ ions.

***5f* magnetism**: In light actinides $5f$ wave function extends more into space in comparison to heavy actinides or lanthanides, where $5f$ wave function is localized. Between these two groups lies uranium in which character of $5f$ wave function can be changed by external variables like pressure, external magnetic field and chemical doping and means we can observe interesting phenomena. The *5f* electron states are delocalized in light actinides because of their participation

in bonding and considerable hybridization with the valence states of neighboring atoms.

This has serious consequences. The most important one is that the *5f* states form a more or less narrow *5f* band intersected by the Fermi energy E_F rather than discrete energy levels. Consequently, the magnetic moments due to the delocalized *5f* electrons are considerably smaller than expected for free ion.

In heavy elements like actinides spin-orbit interaction becomes very strong. As a consequence orbital moment can be induced even in case of considerably delocalized $5f$ electrons and huge magnetocrystalline anisotropy with easy magnetization direction by rule perpendicular to strongly bound $5f$ orbitals.

In case of strong delocalization the *5f* electron magnetic moment completely disappears. The strength of the exchange interaction between corresponding *5f* moments in actinide intermetallic is much stronger than for the *4f* moments interacting only via RKKY interaction.

Hill limit Generally two one-electron mechanisms can be considered affecting the ionic character of the *5f* states. The first one is the *5f* electron hopping due to an overlap of the *5f* wave functions with neighboring U atoms leading to formation of the *5f* band and their delocalization. In this mechanism the U-U spacing (the distance between centers of two nearest uranium ions) is the crucial parameter. In uranium compounds with small U-U spacing ($d_{\text{U-U}}$) non-magnetic, frequently superconducting ground state is found, whereas for larger $d_{\text{U-U}}$ the ground state is often magnetic. The critical value for $d_{\text{U-U}}$ where the character breaks is known as Hill's limit and is empirically considered to be between 340 and 360 pm. This rule applies for pure uranium and uranium rich compounds and many exceptions can be shown in which the hybridization of the *5f* electron states with valence electron states of neighboring atoms (*5f*-ligand hybridization) plays a crucial role (Figure 2.6) [10].

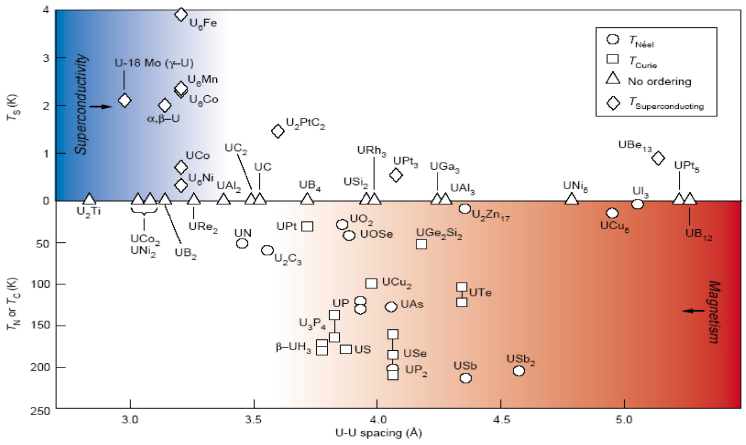

Figure 2.6: Hill's plot

2.2 Quantum phase transitions and quantum critical point

At nonzero temperatures we distinguish two types of phase transitions. To determine type of phase transition we describe each phase by order parameter as proposed by Landau. First order phase transition is described as discontinuous vanishing of order parameter at the transition point. As for second order (continuous) phase transition parameter vanishes continuously at the transition temperature.

Transitions from paramagnetism to magnetic order or from metallic state to superconducting are mostly classified as continuous phase transition. To understand continuous phase transition lets consider Heisenberg ferromagnet, where transition from paramagnetism to ferromagnetism occurs [11]. Order parameter in this system can be described by using magnetization. Let our order parameter be M, than for two points in space we have

$$\langle M(x)M(y)\rangle = f\left(|x-y|/\xi\right) \tag{2.29}$$

where f is function depending on spatial distance between x and y and correlation length ξ. Approaching critical point correlation length diverges, usually like a power law and can be characterized as

$$\xi \propto t^{-\nu} \tag{2.30}$$

where ν is correlation length critical exponent and t is dimensionless parameter characterizing distance from critical point. For transition at nonzero T_{C}, we can use $t = |T - T_{\mathrm{C}}|/T_{\mathrm{C}}$ as dimensionless parameter. At criticality, when correlation length diverges, order parameter correlations decay as power law. This power law is

$$\langle M(x)M(y)\rangle_{t=0} \propto |x-y|^{-d-2+\eta} \tag{2.31}$$

where η is critical exponent and d denotes spatial dimensionality of the system.

Similarly to correlation in space, we can describe effects in temporal behavior of system. We can describe time it takes system to return to equilibrium state after some perturbation as equilibration time τ_{C}. As we approach criticality equilibration time starts to diverge and behaves like a power of correlation length

$$\tau_{\mathrm{C}} = \propto \xi^{z} \tag{2.32}$$

where z is critical exponent. We can define critical frequency scale, which goes to zero as criticality is approached as

$$\omega_{\mathrm{C}}\left(t \to 0\right) \propto 1/\tau_{\mathrm{C}} \to 0. \tag{2.33}$$

Critical exponents z, ν and η characterize the power law behavior of various observables near critical point. Other critical exponents β, γ and δ. β describes vanishing of the order parameter

$$M\left(t \to 0\right) \propto t^{\beta}. \tag{2.34}$$

γ describes divergency of the order parameter susceptibility. In our case defined as $\chi = M/B$

$$\chi\left(t \to 0\right) \propto t^{-\gamma} \tag{2.35}$$

and δ describes dependency of the order parameter on its conjugate field, which in our case is external magnetic fiield B

$$M\left(t \to 0, B \to 0\right) \propto B^{1/\delta}. \tag{2.36}$$

This critical exponents are related to each other by scaling laws or exponent relations. Critical exponents are same for similar phase transition. This is called universality behavior.

For thermal phase transition quantum mechanics is not concerned, because of low energy of quantum oscillations. For low temperatures we can consider characteristic energy, for us $\hbar\omega_{\mathrm{C}}$ [11]. If this energy is larger than $k_{\mathrm{B}}T$, then quantum mechanics will be important. If we consider classical thermal phase transition, than dynamical and statistical parts can be decoupled. On the other hand if we consider quantum mechanics, then statistical and dynamical parts are coupled and quantum transition in d spatial dimensions resembles thermal phase transition in $d_{\mathrm{eff}} = d+z$. Phase transition at 0 K behave quantum mechanically and are called quantum phase transitions (QPT) [12]. This QPT can be approached by varying non-thermal parameter p like pressure, chemical composition or external magnetic field. Critical points δ_{c}, where we quantum mechanics dominates are are called quantum critical points (QCP). It was shown by Suzuki in [13], that behavior in QCP can be also observed in small non-zero temperatures near QCP.

Experiments and theoretical development in the last decade has made clear that presence of such QPT plays important role in unsolved problems of heavy-fermion compounds. New properties arise like non-Fermi-liquid behavior and unconventional superconductivity. The temperature dependencies strongly depends on dimensionality of the system and nature of interactions in the system. Schematics phase diagram is shown in Figure 2.7.

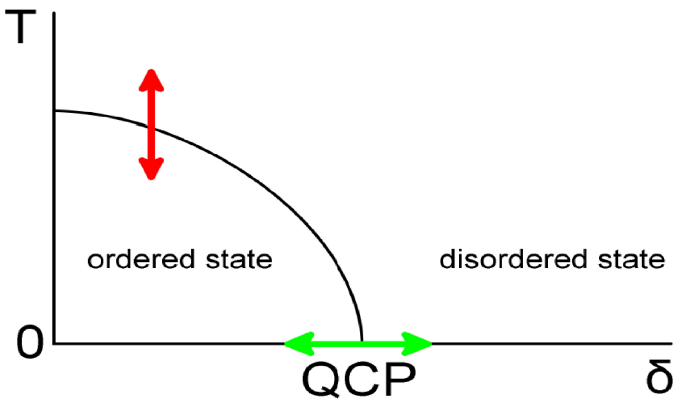

Figure 2.7: Schematic phase diagram showing ordered and disordered state. Red arrow represents classical phase transition. Quantum phase transition at zero temperature is represented by green arrow.

2.3 Electrical resistance

Electrical resistance is defined as [14]

$$\rho = \frac{m}{ne^2\tau} \tag{2.37}$$

where m is mass of electron, e is a charge of electron, n is density of electrons per unit volume and τ is mean free time of electron. In metals contribution of different effects to electrical resistance is additive and is called Matthiessen's rule. Total electric resistivity ρ_{tot} can be divided into four contributions

$$\rho_{\text{tot}} = \rho_0 + \rho_{\text{ph-e}} + \rho_{\text{e-e}} + \rho_{\text{spd}} \tag{2.38}$$

where ρ_0 residual resistivity, $\rho_{\text{ph-e}}$ is electron-phonon scattering, $\rho_{\text{e-e}}$ is electron scattering and ρ_{spd} is scattering due to spin disorder.

Residual resisitivity is temperature independent. It originates from defects in lattice and foreign atoms and phases.

Electron-phonon scattering is due to the thermal motion of atoms and electrons scattering on them, because of this it is thermal dependent. It can be described by [15]

$$\rho_{\text{ph-e}} = A\left(\frac{T}{\Theta_{\text{R}}}\right)^n \int_0^{T/\Theta_{\text{R}}} \frac{x^n}{(e^x - 1)\,(1 - e^{-x})} dx \tag{2.39}$$

where T is temperature, A is constant typical for particular metal and Θ_{R} is Debye temperature. Constant n have different values depending on dominant scattering mechanism. For simple metals we have $n = 5$, for transition metals $n = 3$ and in high temperatures this term is linear for all cases and dominates.

Electron-electron scattering behaves like $\sim A_{\text{ee}}T^2$, where A_{ee} is proportional to square number of electrons at Fermi energy [15]. It is dominant in transition metals thanks to the s-d interband scattering at low temperatures.

Spin disorder scattering is independent on temperature above $T_{\text{C}}\,(T_{\text{N}})$ and below slowly decreases thanks to the ordering [15].

3. Physics of UCoAl

UCoAl belongs to UTX family of compounds, where T stands for transition metal and X for p-metal. Compounds from this family crystallize in orthorombic Ti-Ni-Si structure or hexagonal Zr-Ni-Al structure. UCoAl belongs to latter one [10]. Zr-Ni-Al structure (Figure 3.1) is layered system of U-$T1$ and $T2$-X layers, where $T1$ and $T2$ are nonequivalent positions for transition metal. The structure is responsible for huge magnetocrystalline anisotropy between the c-axis and basal plane, where basal plane is typically isotropic. The shortest distance between two uranium atoms in compounds with ZrNiAl-type structure is always found in the basal plane. Consequently the $5f$ wave functions of uranium mostly interact in basal plane and the $5f$ orbitals are then compressed towards the basal plane. This fact together with the orbital polarization of $5f$ states (due to the strong spin-orbit coupling) leads to magnetic moments oriented parallel to the c-axis, which becomes the easy magnetization axis for most compounds in this family.

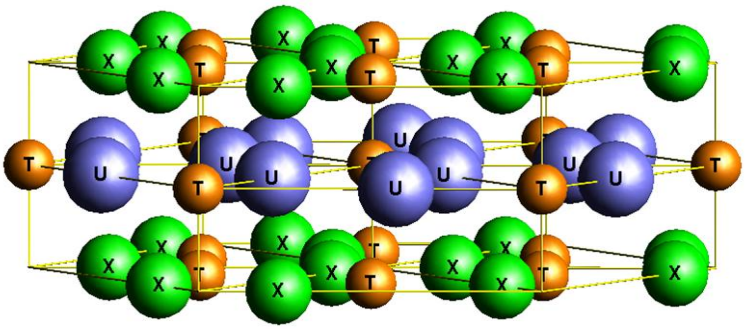

Figure 3.1: Hexagonal UTX structure of Zr-Ni-Al type. For Zr-Ni-Al structure is typical stacking of U-T and T-X planes

UTX family consists of many compounds with interesting physical properties like unconventional superconductivity observed in URhGe and UCoGe[16, 17, 18], both of them crystallize in TiNiSi-type structure. Compounds crystallizing in ZrNiAl-type structure exhibit various types of behavior like paramagnetism, ferromagnetism and antiferromagnetism as shown in Figure 3.2.

UCoAl is paramagnet down to lowest temperatures. By applying external magnetic field of ~ 0.7 T along the c-axis in low temperatures, we observe metamagnetic transition of the first order into itinerant ferromagnetic state [1, 19]. Huge magnetocrystalline anisotropy is preserved even in paramagnetic state. Broad maximum in magnetic susceptibility is observed around 20 K and no considerable anomaly is observed in electrical resistance and heat capacity around this temperature. This broad peak is connected to metamagnetism similarly as in $LuCo_2$ and YCo_2 [20]. Metamagnetic transition changes from crossover regime to first-order transition at critical endpoint (CEP) at 11 K [19]. CEP temperature is suppressed and critical field is increased by applying hydrostatic pressure. Magnetic phase diagram was drafted up by Aoki et al. [21] and is shown in Figure

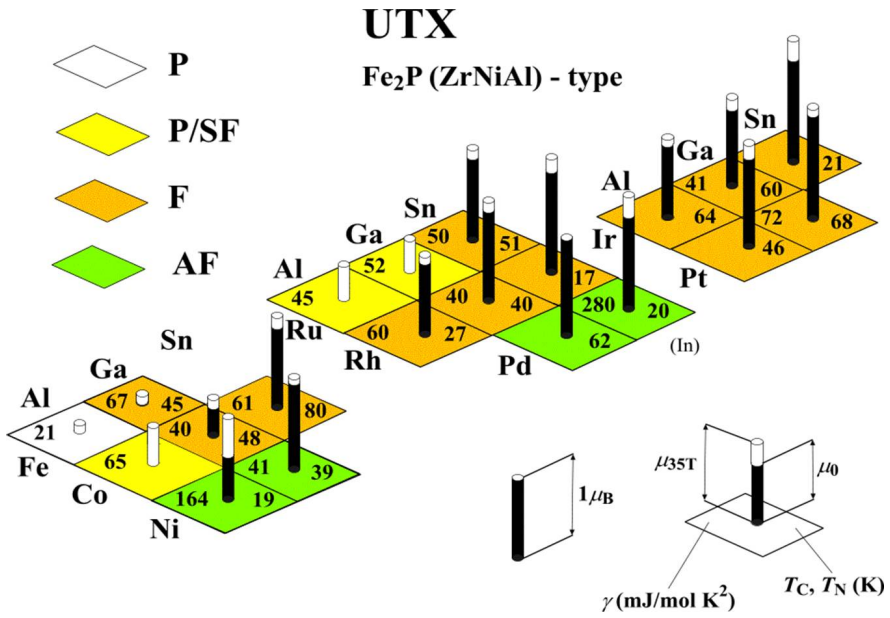

Figure 3.2: Magnetic characters of UTX compounds of ZrNiAl-type [10].

3.3. In this phase diagram ferromagnetism appears in p = -0.2 GPa and CEP dissapears in quantum critical endpoint (QCEP) in 1.5 GPa and 7 T [21].

Different doped compounds of UCoAl, where doped ion was on uranium, cobalt or aluminum sites were focus of research. One of the most interesting is $UCo_{1-x}Ru_xAl$, where both UCoAl and URuAl are paramagnetic but for already $x = 0.01$ ferromagnetism appears and disappears for $x = 0.81$ [3].

Compounds with similar phase diagram as UCoAl are often called quantum itinerant ferromagnets. Compared to antiferromagnets, where Néel temperature is suppressed by tuning parameter into quantum critical point, weak ferromagnets behave differently as was shown by Belitz et al. [2]. They calculated generic phase diagrams shown in Figure 3.4. As can be seen four different phase diagrams exist depending on compound and sample quality. By changing tuning parameter like pressure, external magnetic field or chemical doping, we reach different points in these phase diagrams. Phase diagram a) in Figure 3.4 is case for UCoAl. At this phase diagram second order transition from paramagnetic to ferromagnetic state is suppressed and at tricritical point (TCP) it is changed into first order one and further on is dramatically suppressed by tuning parameter as shown in Figure 3.4a) [22]. Also at TCP wings of metamagnetic first order transition appear and by further tuning disappear in QCEP. Examples of quantum itinerant magnets are UGe_2, URhGe, URhAl and $ZrZn_2$[23, 22, 24, 25]. Figure 3.4b) is typical for strongly disordered or quasi-onedimensional systems. In this phase we do not observe a continuous quantum phase transition. For some systems transitions from ferromagnetic order to modulated spin-density-wave or antiferromagnetic order is observed (Figure 3.4c)). Strongly disordered systems often show spin-glass like behavior in the tail of phase diagram (Figure 3.4d)).

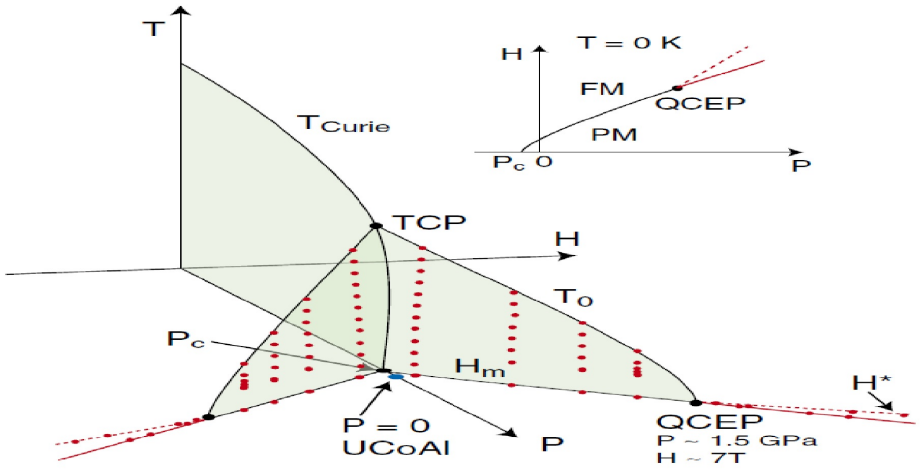

Figure 3.3: UCoAl phase diagram. H_{m} is critical field and H^* is phase above QCEP [21].

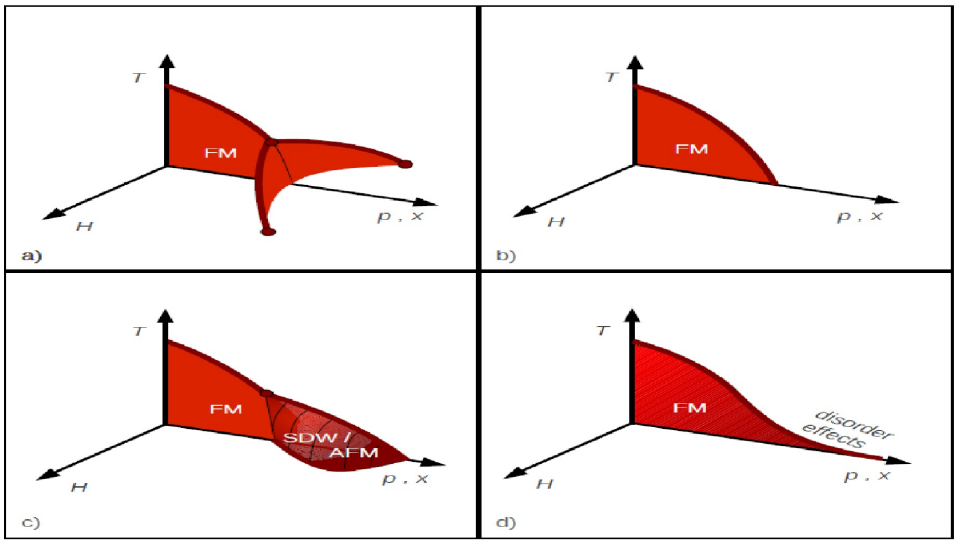

Figure 3.4: Generic phase diagrams for quantum itinerant ferromagnets [22].

4. Experimental methods

4.1 Sample preparations

Polycrystalline precursors were prepared by melting. For melting we used a monoarc furnace with copper crucible and tungsten electrode. Stochiometric amount of elements were put into a crucible. The monoarc chamber was evacuated up to 10^{-6} to 10^{-7} mbar and walls were simultaneously heated. To melt elements we filled chamber with high purity argon (6N), which functions as protective atmosphere and charge carrier. To achieve better homogeneity, precursor is flipped and remelted several times.

4.1.1 Czochralski method

One of the most used techniques for single crystal growth nowadays is Czochralski method. It is used for various conductive materials. At beginning precursor is melted in crucible and seed rod is inserted inside. As a seed rod a single crystal of desired product can be used or other material with high melting point. Seed rod is then pulled up from 2 to 15 millimeters per hour, while melt crystallize on rod. Seed rod and melt are rotating in opposing directions. The main control parameter of growth is the temperature of melt. By heating it up we decrease the diameter and start "necking procedure". During this only one grain is selected to achieve single crystal. After this the temperature of melt is lowered to increase diameter. Success of whole procedure depends on many parameters and makes it difficult.
Our samples were prepared home-made tri-arc furnace, where melting is done by three tungsten electrodes and precursor is placed on water cooled copper crucible. As seed rod we used tungsten rod. Whole growth procedure is done argon protective atmosphere.

4.1.2 Sample annealing

Single crystals after growth contain many mechanical defects, proper occupancy of the atoms is not achieved and mechanical strain is often presented. This is thanks to fast cooling of the materials in triarc furnace when process is finished. Samples for annealing are wrapped into tantalum foil and placed in quartz tube. The tantalum foil prevents reaction between sample and silicon in tube, which would contaminate the annealed sample. The tube is finally sealed up to 10^{-6} mbar with simultaneous baking of the tube up to 300 °C to desorb gasses. Parameters of the annealing treatment strongly depend on the properties of material – phase diagram, melting point.

4.2 Sample characterization methods

The characterization of samples is very important in material research. Presence of impurities and other phases significantly affects physical properties of

samples. Magnetic measurements can be strongly affected by ferromagnetic impurities. Three methods were used for analysis of samples. Powder X-ray diffraction (XRPD), microprobe analysis - Energy Dispersive X-ray analysis (EDX) for finding impurities and Laue method for determination of quality of single crystal and their orientation.

4.2.1 X-ray methods

X-rays are photons characterized by their wavelength from 0.1 nm to 10 nm. One of the conditions for diffraction on sample is that the wavelength of the X-ray must be of the same order as interatomic distances in sample. In laboratories X-rays are generally generated by X-ray tubes, where accelerated electrons collide with anode target and X-rays are emitted. Different materials (Cu, Fe, Ni, Mo, W etc.) for anode are used, because of their characteristic spectrum. All X-ray methods work on the basis of Bragg's Law [5]

$$2d \sin(\theta) = n\lambda, \tag{4.1}$$

The integer n is the order of corresponding diffraction, λ is the wavelength of the X-rays, θ is Bragg's angle which gives deviation from diffraction planes hkl distanced by d.

X-ray powder diffraction

X-ray powder diffraction is analytical X-ray method used for structural analysis of materials. It is based on the idea, that if we have numerous little grains of the material than there exists one that is oriented in way, that it satisfies (4.1). As result, we get diffractogram which shows dependence of reflected intensity on diffraction angle 2Θ. We have used Bruker AXS D8 Advance X-ray diffractometer with Cu X-ray tube in Brag-Brentano geometry for measuring powder diraction (Figure 4.1). In Brag-Brentano geometry detector and X-ray tube are placed in constant distance from powder sample and angle between source and detector changes accordingly to rotation of sample about the main axis of the diffractometer. The detector rotates with double angular frequency than sample. It secures that the angle between impacted and diffracted beams is the Bragg's angle Θ for the specific hkl diffraction.

To analyze diffraction patterns we used Rietveld method. Approximate structure parameters are used as start parameters. Least square algorithm is used to fit theoretical structure with measured data. Lattice parameters determine positions of difraction peaks and other structure parameters determine shape and intensity. The whole analysis is done by FullProf program [26].

Laue method

Laue method with back reflection geometry was used for determination of quality and orientation of our single crystals. Laue diffractometer made by Photonic Science with Cu X-ray tube and voltage up to 40 kV was used. Laue method works with polychromatic X-ray in which some wavelengths fulfill Bragg's law for given crystal structure. The result is image of reciprocal crystal lattice of the single crystal. The crystals are checked and oriented by placing on goniometer head

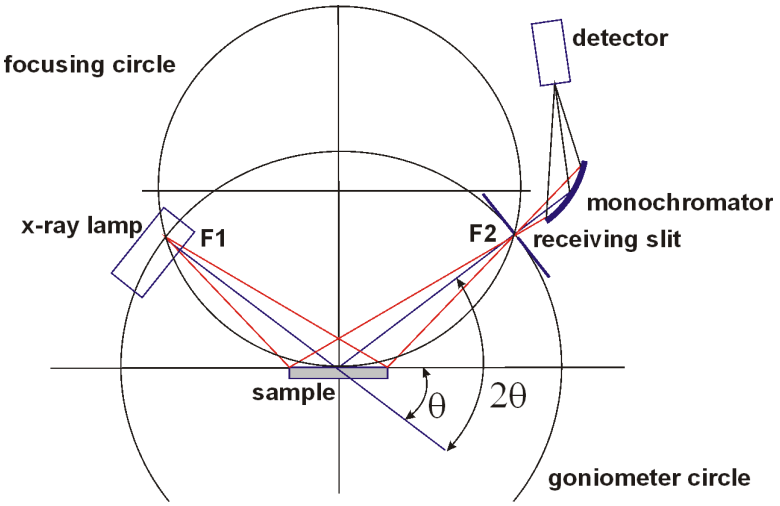

Figure 4.1: Bragg - Brentano geometry of X-ray diffractometer

and rotated to find the desired orientation. Reflection are detected by CCD camera. Scanned image is analyzed using software provided by Photonic Science.

4.2.2 EDX

Scanning electron microscope (SEM) Tescan Mira I LMH [27] was used, where electron beam is produced by Schottky cathode. Two types of detectors are used to produce final image: secondary electrons (SE) and backscattered electrons (BSE) detector. BSE detector is based on scattering of electrons on atom. Intensity of BSE depend on atomic number of target atom. Heavy elements backscatter more electrons which means higher intensity. This can be used to reveal tiny amounts of spurious phases and elements. Energy Dispersive X-ray analysis (EDX) is one of the analysis methods used in SEM. It is used to determine chemical composition of materials. Accelerated electrons can eject electron from its orbitals and then electron from outer shell takes its places simultaneously emitting energy in the form of X-ray photon. This X-rays are than detected. The composition is calculated on the basis of atlas of X-ray spectra implemented in the software. The amount of the each elements is given by intensity of the characteristic lines. Bruker AXS analyzer was used with Esprit software with implemented ZAF correction to calculate composition.

4.3 MPMS

Magnetic Properties Measurement System made by Quantum Design and equipped with SQUID (superconducting quantum interference device) was used to measure magnetization. The sample is positioned in the center of superconducting solenoid and between SQUID detection coils. Temperature between 1.8 K to 400 K can be achieved in sample space. Maximum magnetic field of 7 T can be created by superconducting magnet [28]. The maximum sensitivity of SQUID magnetometer is around 10^{-8} emu.

4.4 PPMS

Physical Properties Measurement System developed by Quantum Designs for measuring physical properties of materials in wide range of temperatures and up to magnetic field of 14 T (our device). Sample can be put in various types of inserts, specific for each measurement. Insert with sample is placed in cooling annulus which is positioned in the center of superconducting magnet. Every insert has universal connector which secures transport of measure data to computer. Detail of sample space arrangement of PPMS is in Figure 4.2.

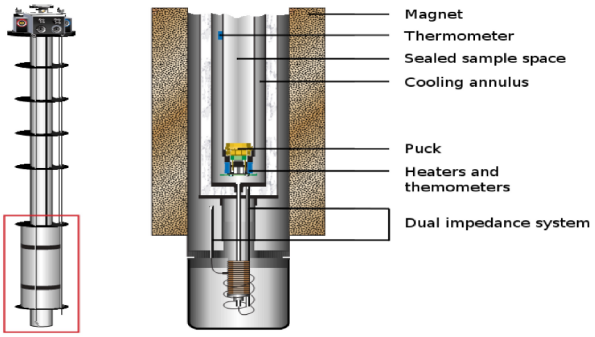

Figure 4.2: Schematic of PPMS probe and detail of lower part [28].

4.4.1 Electric properties measurements

PPMS equipment was used to measure ACT resistivity. The four terminals method was used for measurement with current of resolution of 0.02 μA and maximum value of 2 A, and voltmeter with sensitivity of 1 nV at 1 kHz. The available frequencies of the AC current range from 1 Hz to 1 kHz. The samples in the form of long beam are the best for resistivity measurement. The sample is contacted by four gold wires, where two inner contacts are connected to the voltage detector and two outer contacts are connected to current supply. Special puck for ACT is used and two samples can be measured simultaneously (Figure 4.3). The AC resistivity as function of temperature can be measured from 0.35 K to 400 K and in applied external magnetic field up to 14 T.

Figure 4.3: Puck for ACT measurements [28].

4.5 Pressure cells

Small pressure cell made from CuBe with inner diameter 2.5 mm and external parameter 8.6 mm was used to measure magnetic properties in MPMS up to 1 GPa (Figure 4.4). Hydrostatic pressure inside was determined by known pressure dependence of superconducting transition of lead. Spindle oil was used as pressure medium.

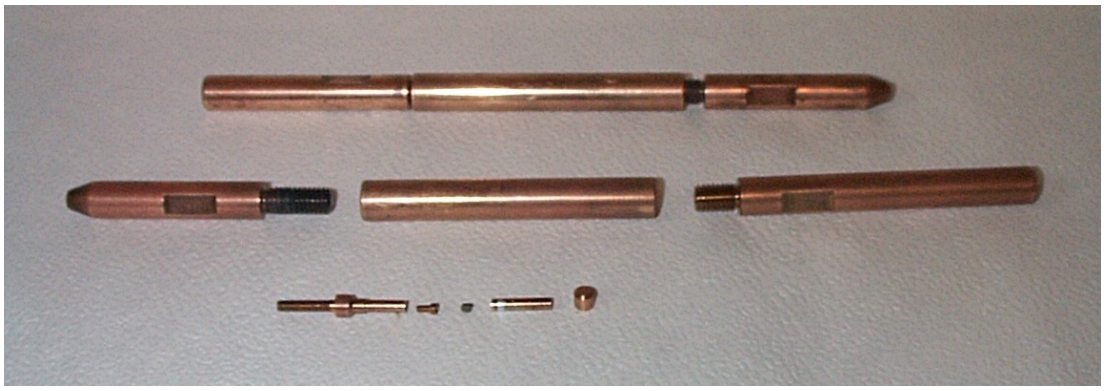

Figure 4.4: CuBe clamp pressure cell used in MPMS [29].

5. Results

5.1 Samples preparation

Three single crystals of nominal compositions $UCo_{0.99}Ru_{0.01}Al$, $UCo_{0.995}Ru_{0.005}Al$ and $UCo_{0.9975}Ru_{0.0025}Al$ have been grown. Polycrystalline precursors of mass ~ 11 g were prepared and single crystals were grown by Czochralski method in the triarc furnace. Tungsten rods were used as the seed rods. The grown single crystals had diameter between 2.5 mm to 3 mm and length from 1 cm to 2 cm. Single crystals were then wrapped in tantalum foil and annealed for 5 days in 900°C.

5.2 Single crystals characterization

5.2.1 Laue method

Quality of all single crystals was verified by Laue method. No spurious phases, twins or polycrystals were found. All single crystals were oriented with respect to crystallographic axes for further measurements. Example of diffractogram taken by Laue method is in Figure 5.1.

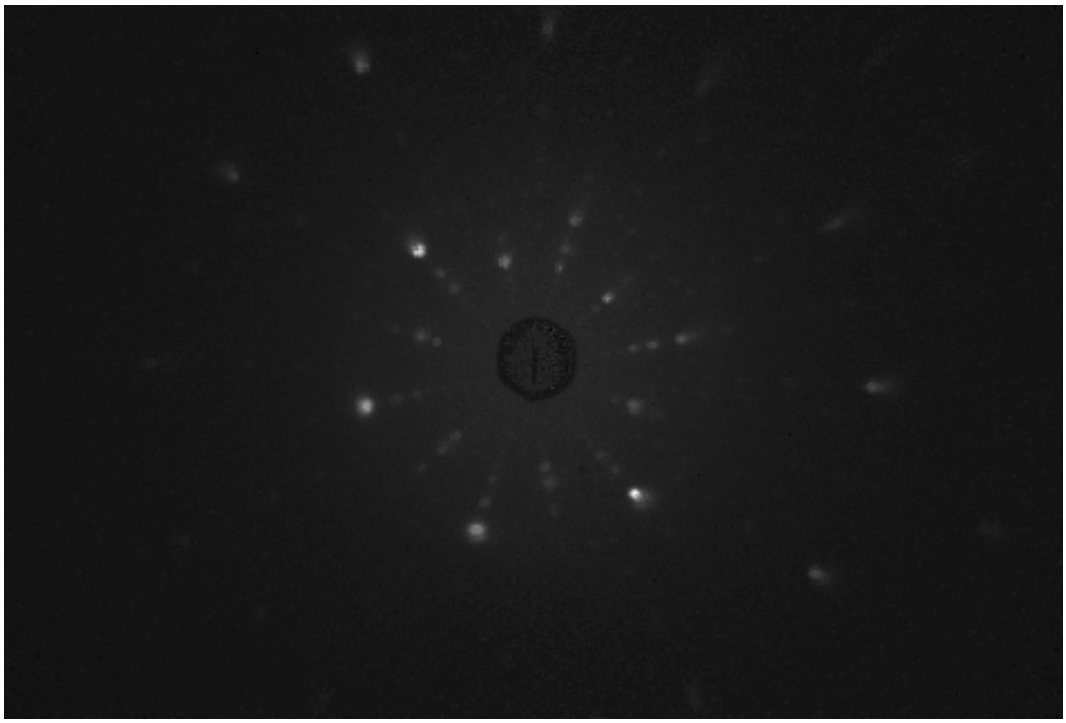

Figure 5.1: Diffractogram from Laue method of $UCo_{0.995}Ru_{0.005}Al$. The c-axis is perpendicular to picture.

5.2.2 EDX analysis

Small pieces from opposite ends (with respect to direction of growth) of single crystals $UCo_{0.995}Ru_{0.005}Al$ and $UCo_{0.9975}Ru_{0.0025}Al$ and piece of $UCo_{0.99}Ru_{0.01}Al$ were cut and polished for EDX analysis (Figure 5.2). No other phases were found in all single crystals. EDX analysis of all single crystals show same composition of $UCo_{0.98}Ru_{0.02}Al$.

The virtually ambiguous result can be conceived having in mind that the sensitivity of the EDX detector is on the level of 1-2 % and the actual Ru concentration in the studied crystals is below.

In this situation the nominal compositions were taken for further consideration and confronted with the evolution of magnetism.

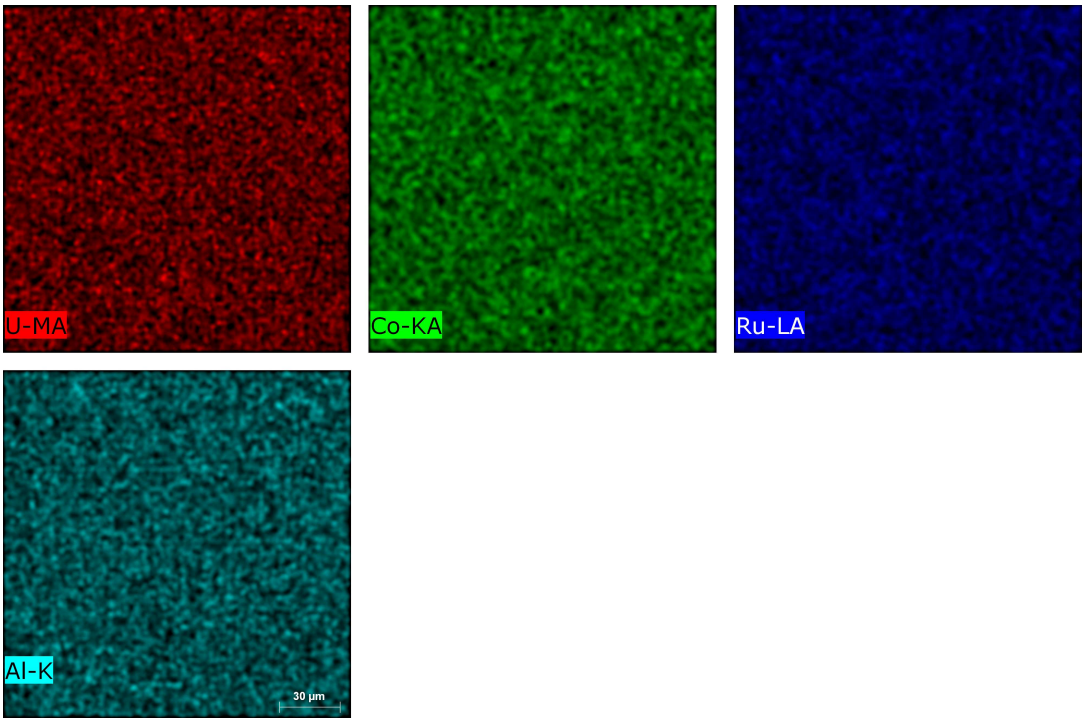

Figure 5.2: Picture of map scan from EDX analysis taken by BSE detector of $UCo_{0.995}Ru_{0.005}Al$.

5.2.3 Results of XRPD

Parts of single crystals were pulverized with agate mortar and pestle into polycrystalline powder. Results for all crystals are in Table 5.1. Due to low ruthenium concentration we were not able to determine occupancy of transition metal positions. We can see that c-axis shows no change with substitution. We observe increase in the basal plane. This means larger distance between nearest neighboring uraniums and also larger distance between uranium and transition metal. We can expect smaller hybridization of the $5f$ electron states with electron states of neighboring atoms in basal plane, because of this.

Table 5.1: Cell parameters for $UCo_{1-x}Ru_xAl$. Data for UCoAl were taken from [30].

	x = 0.01	x = 0.005	x = 0.0025	x = 0
a [Å]	6.6887(2)	6.6875(2)	6.6867(1)	6.686
c [Å]	3.9660(2)	3.9664(2)	3.9668(1)	3.966

5.2.4 Analysis by magnetic measurements

Samples for measurements were chosen in same way as for EDX analysis. Measurements were done using MPMS. The three single crystals showed different magnetic behavior and no sign of gradient effect in any single crystal was observed. To distinguish between different single crystals we will use nominal composition to differentiate between them. Detailed results of magnetic measurement are shown in following sections.

The three single crystals show strong magnetocrystalline anisotropy with the c-axis being the easy magnetization axis.

5.3 $UCo_{0.99}Ru_{0.01}Al$ single crystal study

5.3.1 Magnetization measurements

The almost rectangular hysteresis loop recorded at 1.8 K (see Figure 5.3) confirms that this compound is ferromagnetic at low temperatures. Detailed analysis of the magnetization curves (Figure 5.3) and the thermomagnetic curve measured in low magnetic field (Figure 5.4a)) suggests a transition from paramagnetic state to a ferromagnetic state is observed at $T_C = 16$ K.

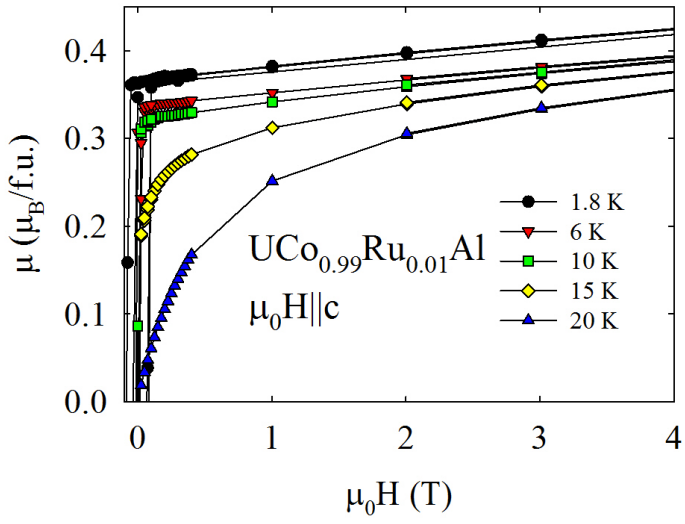

Figure 5.3: Hysteresis loops in different temperatures for $UCo_{0.99}Ru_{0.01}Al$. Hysteresis loop at 1.8 K has typical rectangular shape for ferromagnets.

Temperature dependence of magnetization shows no anomaly around 20 K

characteristic for UCoAl (Figure 5.4a)). This is consistent with disappearance of metamagnetic transition thanks to onset of ferromagnetic ordering.

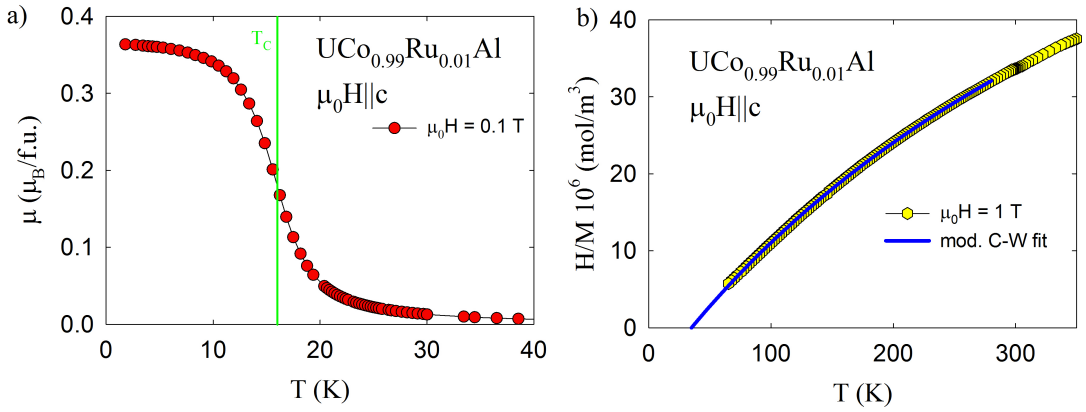

Figure 5.4: Temperature dependence of a)magnetization and b)susceptibility for $UCo_{0.99}Ru_{0.01}Al$.

Temperature dependence of magnetic susceptibility was fitted above 80 K by modified Curie-Weiss (CW) law (Figure 5.4b)). Resulting parameters are $\chi_0 = 9.75 \cdot 10^{-9}\mathrm{m}^3 \cdot \mathrm{mol}^{-1}$, paramagnetic Curie temperature $\Theta_\mathrm{P} = 34.9$ K and effective magnetic moment $\mu_\mathrm{eff} = 1.83\ \mu_\mathrm{B}$/U ion. Results are similar to those for pure UCoAl [1]. Moment per uranium ion is much smaller than the values expected for free U^{3+} or U^{4+} ion, respectively. This is due to the delocalization of $5f$ electrons, which mainly comes from hybridization overlap of $5f$ orbitlas of nearest U neighbors and of $5f$ states with neighboring d states of transition metal [10].

5.4 $UCo_{0.995}Ru_{0.005}Al$ single crystal study

5.4.1 Magnetization measurements

The shape of hysteresis loops is unusual. In low fields they show some hysteresis, especially visible at 1.8 K and 4.5 K, but in higher fields resembling metamagnetic behavior (Figure 5.5). At higher temperatures we see only metamagnetic behavior.

From detailed analysis of magnetization curves and the low-field thermodynamic curve the Curie temperature
$T_\mathrm{C} = 4.5$ K has been determined. In Figure 5.6a) one can see anomaly around 17 K similar to the 20 K anomaly for to UCoAl [1]. This suggest coexistence of ferromagnetism and metamagnetism in low temperatures. This coexistence is discussed in chapter General discussion.

Temperature dependence of paramagnetic part of magnetic susceptibility of $UCo_{0.995}Ru_{0.005}Al$ was fitted by modified CW law (Figure 5.6b)). Parameters of fit are $\chi_0 = 6.96 \cdot 10^{-9}\mathrm{m}^3 \cdot \mathrm{mol}^{-1}$, paramagnetic Curie temperature $\Theta_\mathrm{P} = 31.6$ K and effective magnetic moment $\mu_\mathrm{eff} = 1.87\ \mu_\mathrm{B}$/U ion. Resulting parameters are similar to those for $UCo_{0.99}Ru_{0.01}Al$ and for pure UCoAl [1].

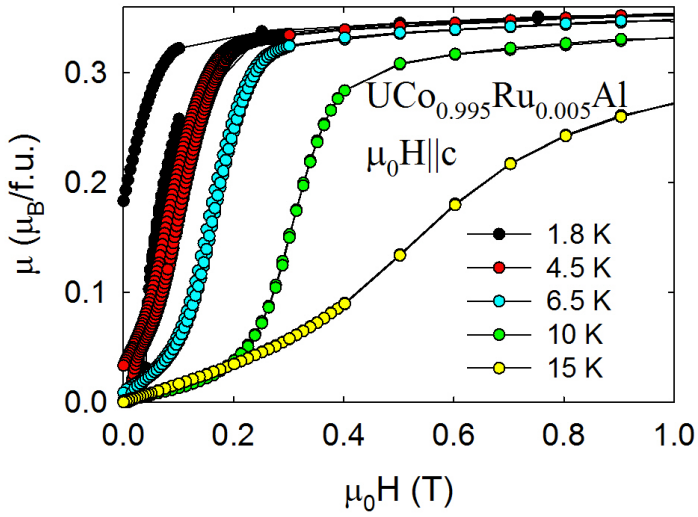

Figure 5.5: Hysteresis loops in different temperatures for $UCo_{0.995}Ru_{0.005}Al$.

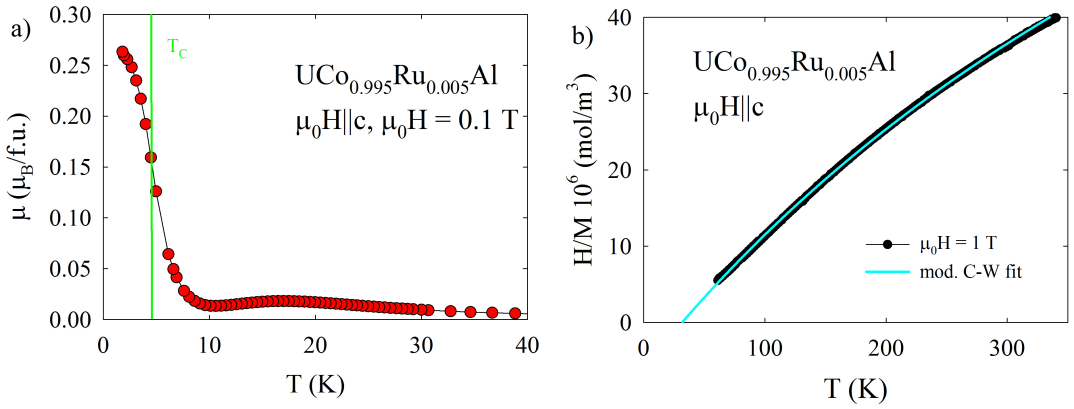

Figure 5.6: Temperature dependence of a) magnetization and b) susceptibility for $UCo_{0.995}Ru_{0.005}Al$. The anomaly around 17 K is similar to the 20 K anomaly for UCoAl.

5.4.2 Electric resistivity measurements

Electric resistivity was measured using ACT transport option in PPMS with electric current in basal plane and magnetic field along the c-axis. $UCo_{0.995}Ru_{0.005}Al$ has $RRR = 9$ with residual resistivity $\rho_0 = 15\mu\Omega \cdot$ cm. Temperature dependence of electric resistivity in Figure 5.7 shows progressive decrease with increasing external magnetic field applied along the c-axis. This points to existence of spin fluctuations similar to UCoAl [31]. Magnetoresistivity in Figure 5.8 shows steep decrease in low fields and change of slope at metamagnetic transition. Compared to UCoAl, $UCo_{0.995}Ru_{0.005}Al$ does not show in fields below the critical field, because of the small critical field.

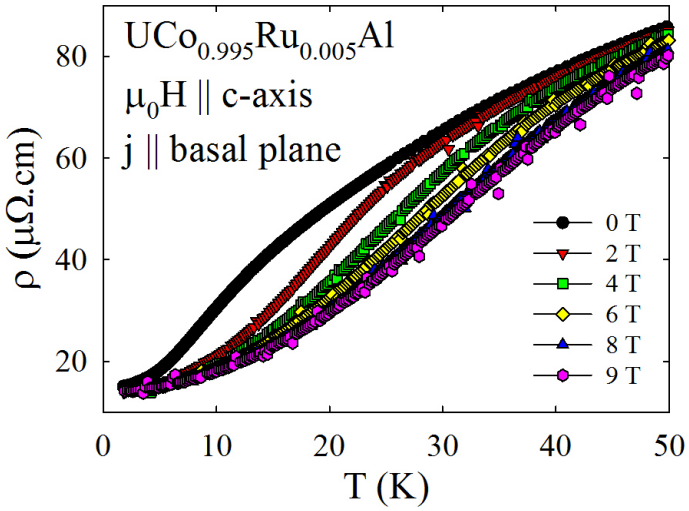

Figure 5.7: Temperature dependence of electric resistivity of $UCo_{0.995}Ru_{0.005}Al$.

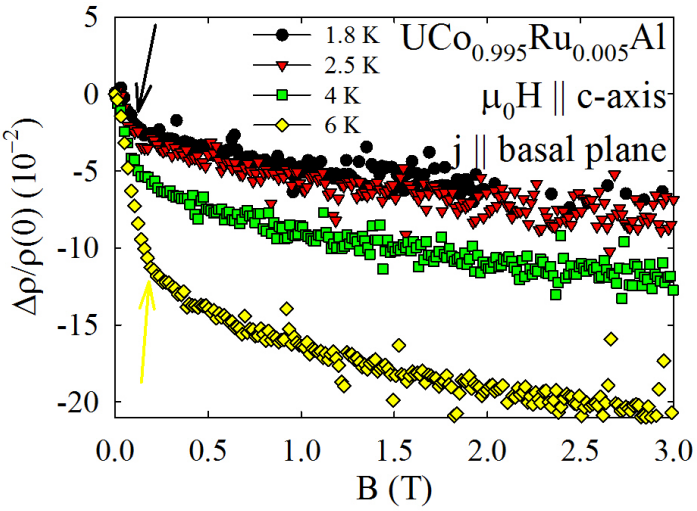

Figure 5.8: Magnetoresistivity of $UCo_{0.995}Ru_{0.005}Al$. Arrows indicate where metamagnetic transition occurs in respect of their colors.

5.5 $UCo_{0.9975}Ru_{0.0025}Al$ single crystal study

5.5.1 Magnetization measurements

$UCo_{0.9975}Ru_{0.0025}Al$ is paramagnetic down to 1.8 K. The metamagnetic transition is observed in 0.55 T (Figure 5.9). The critical field of $UCo_{0.9975}Ru_{0.0025}Al$ is smaller than for pure UCoAl [1]. An anomaly around 17 K is observed in the

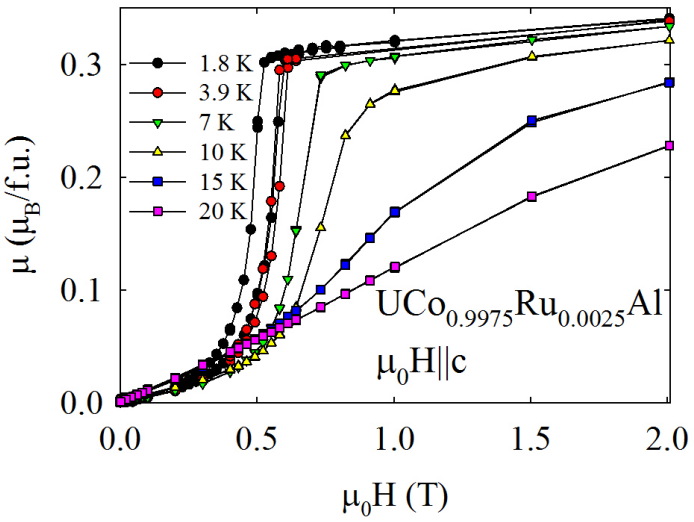

Figure 5.9: Hysteresis loops in different temperatures for $UCo_{0.9975}Ru_{0.0025}Al$.

temperature dependence of magnetization, similar to $UCo_{0.995}Ru_{0.005}Al$ and the 20 K anomaly for UCoAl (Figure 5.10a)).

Paramagnetic part of temperature dependence of magnetic susceptibility was fitted with modified CW law. The resulting parameters are $\chi_0 = 6.88 \cdot 10^{-9} \mathrm{m}^3 \cdot \mathrm{mol}^{-1}$, paramagnetic Curie temperature $\Theta_\mathrm{P} = 33.3$ K and effective magnetic moment $\mu_\mathrm{eff} = 1.83\ \mu_\mathrm{B}$ (Figure 5.10b)). Results are similar to those for the other two single crystals and UCoAl.

5.5.2 Electric resistivity measurements

The electric resistivity of $UCo_{0.9975}Ru_{0.0025}Al$ was measured in same way as in the previous case. The temperature dependence resembles behavior of $UCo_{0.995}Ru_{0.005}Al$, which points to similar role of spin fluctuations (Figure 5.11). Magnetoresistivity shows similar behavior as in UCoAl (Figure 5.12). At the metamagnetic transition change of a slope occurs, similarly to $UCo_{0.995}Ru_{0.005}Al$. The residual resistivity ratio $RRR = 6$ while residual resistivity $\rho_0 = 40\mu\Omega \cdot \mathrm{cm}$, which is larger than $UCo_{0.995}Ru_{0.005}Al$.

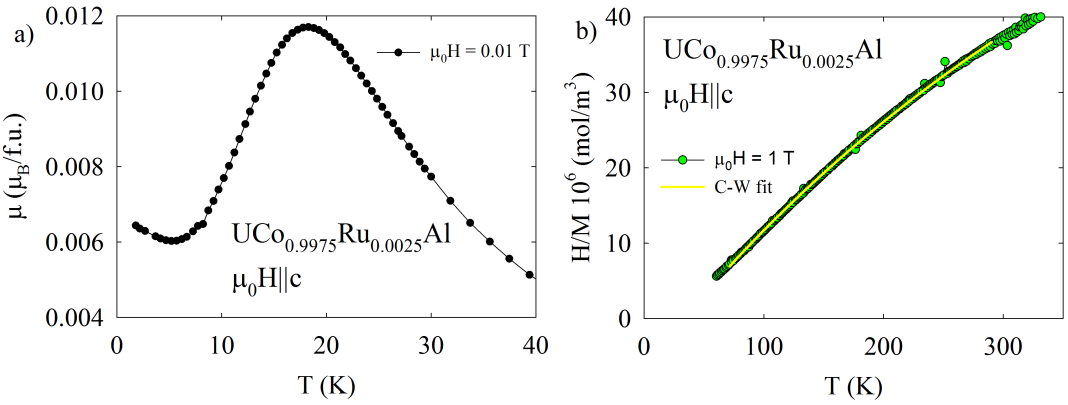

Figure 5.10: Temperature dependence of a) magnetization and b) susceptibility for $UCo_{0.9975}Ru_{0.0025}Al$. Anomaly around 17 K, similarly to UCoAl.

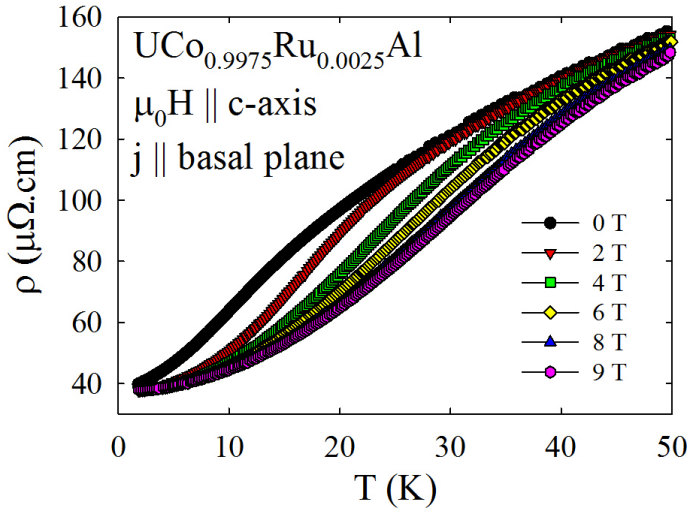

Figure 5.11: Temperature dependence of electric resistivity of $UCo_{0.9975}Ru_{0.0025}Al$.

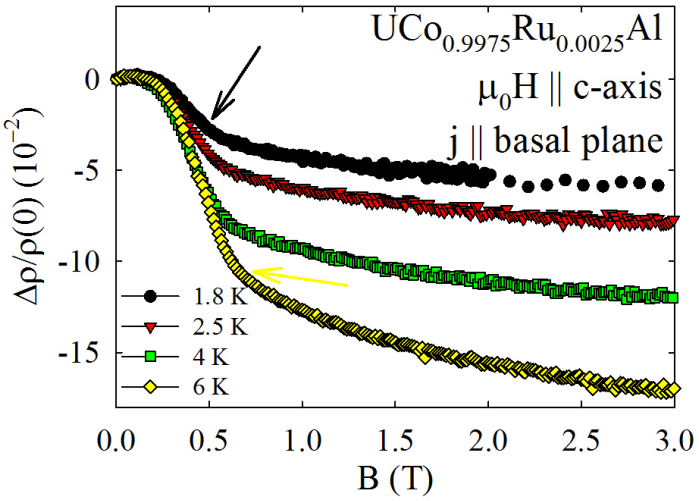

Figure 5.12: Magnetoresistivity of $UCo_{0.9975}Ru_{0.0025}Al$. Arrows indicate where metamagnetic transition occurs in respect of their colors.

5.6 Magnetization measurements in hydrostatic pressure

Magnetic properties were measured using CuBe pressure cell for a MPMS. Single crystals of $UCo_{0.995}Ru_{0.005}Al$ and $UCo_{0.9975}Ru_{0.0025}Al$ were measured along the c-axis with external magnetic field applied along same direction. Pressure was determined from superconductivity transition of lead.

5.6.1 $UCo_{0.995}Ru_{0.005}Al$

$UCo_{0.995}Ru_{0.005}Al$ was measured in four different pressure including ambient pressure. Hysteresis loops in Figure 5.13 show increase of critical field and decrease of saturated moment with increasing pressure. We also observe disappearance of ferromagnetism already in 0.46 GPa. From derivative of hysteresis loops at a critical field we determined temperatures of CEPs (T_0), which are shown in Table 5.2 with critical fields. Phase diagram of $UCo_{0.995}Ru_{0.005}Al$ is shown in Figure 5.14, which shows similar temperature dependence of the critical field in all pressures. $UCo_{0.995}Ru_{0.005}Al$ shows similar behavior to UCoAl, suggesting phase diagram with wing structure.

For first pressure point of 0.24 GPa we observe similar behavior to ambient pressure. Determination of low pressures from lead's superconductivity transition carries large error and in our case it was also screened by ferromagnetic transition connected to $UCo_{0.995}Ru_{0.005}Al$.

5.6.2 $UCo_{0.9975}Ru_{0.0025}Al$

$UCo_{0.9975}Ru_{0.0025}Al$ was measured similarly as $UCo_{0.995}Ru_{0.005}Al$ and shows similar behavior, as can be seen from Figure 5.15. Temperatures of CEPs were determined in same way as for $UCo_{0.995}Ru_{0.005}Al$ and they are shown Table 5.3

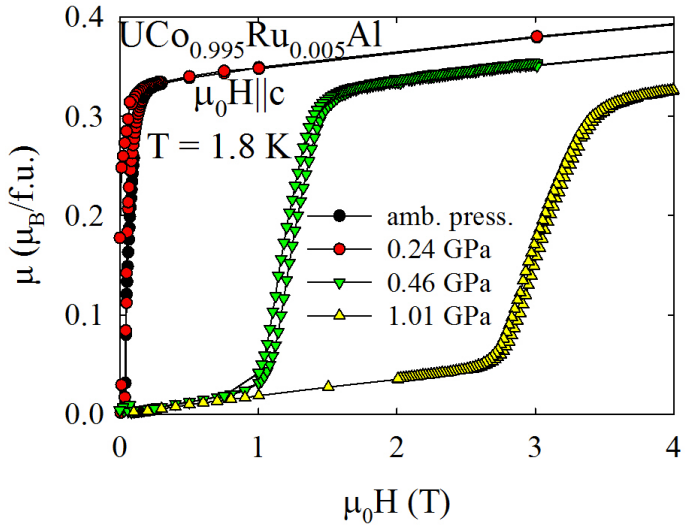

Figure 5.13: Hysteresis loops of $UCo_{0.995}Ru_{0.005}Al$ in 1.8 K in different hydrostatic pressures.

Table 5.2: Critical fields and critical temperatures for $UCo_{0.995}Ru_{0.005}Al$ in different pressures.

P (GPa)	T_C (K)	T_0	H_C at 1.8 K	H_C at T_0
0	4.5	11	0.040	0.350
0.24	4.5	11	0.040	0.350
0.46	-	9.6	1.237	1.405
1.01	-	8	2.984	3.119

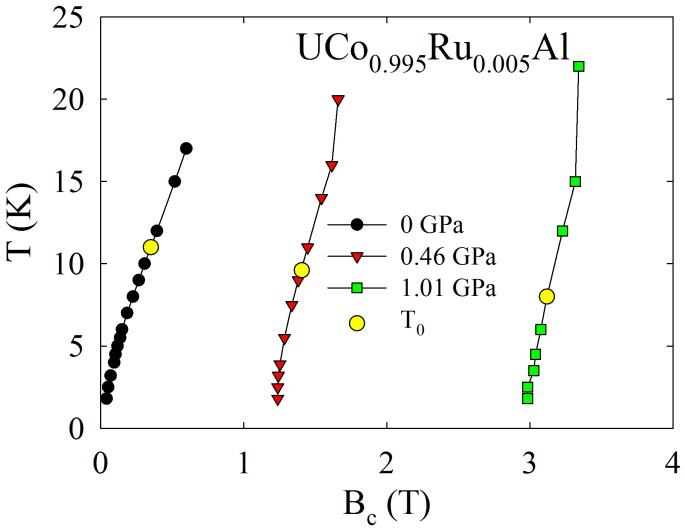

Figure 5.14: Phase diagram of $UCo_{0.995}Ru_{0.005}Al$ in different hydrostatic pressures. Yellow points are for the temperatureT_0 of CEP in different pressures.

with critical fields. Phase diagram of $UCo_{0.9975}Ru_{0.0025}Al$ is shown in Figure 5.16, which shows similar temperature dependence of the critical field in all pressures. Behavior of $UCo_{0.9975}Ru_{0.0025}Al$ suggest phase diagram with wing structure similar to pure UCoAl.

Similar to $UCo_{0.995}Ru_{0.005}Al$, first pressure point has large error. Difference between hysteresis loops in ambient pressure and in 0.16 GPa in Figure 5.15 is due to change of sample orientation.

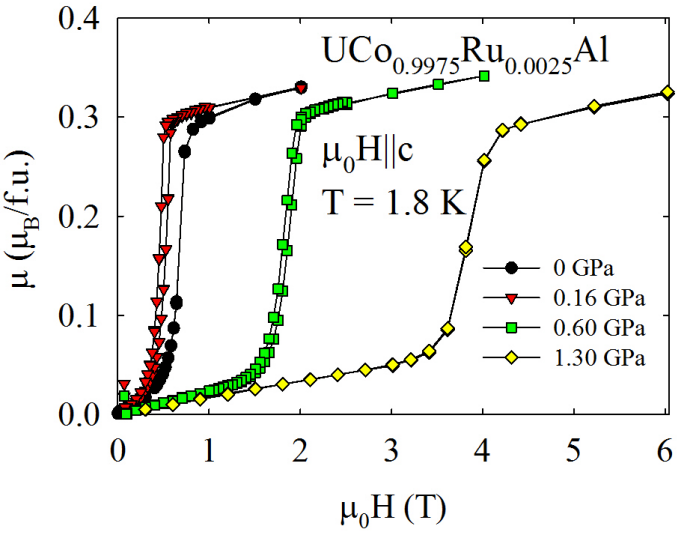

Figure 5.15: Hysteresis loops of $UCo_{0.9975}Ru_{0.0025}Al$ in 1.8 K in different hydrostatic pressures.

Table 5.3: Critical fields and critical temperatures for $UCo_{0.9975}Ru_{0.0025}Al$ in different pressures.

P (GPa)	T_0	H_C at 1.8 K	H_C at T_0
0	10.5	0.550	0.760
0.16	10.5	0.550	0.760
0.6	8.5	1.902	1.946
1.3	6.5	3.836	3.870

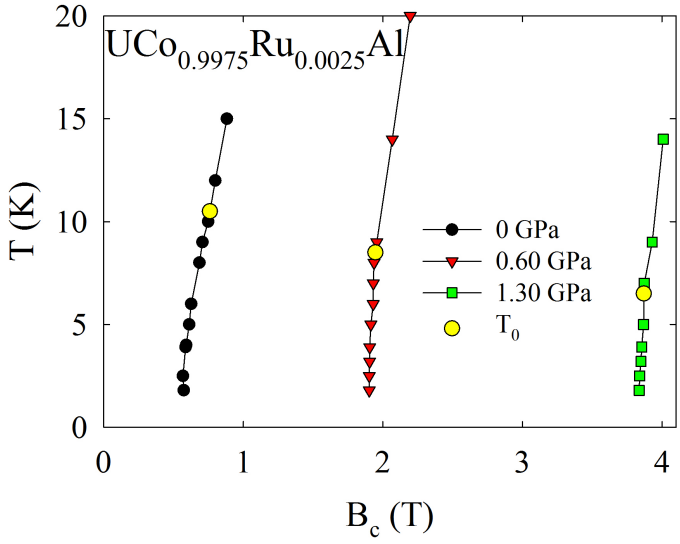

Figure 5.16: Phase diagram of $UCo_{0.9975}Ru_{0.0025}Al$ in different hydrostatic pressures. Yellow points are for the temperature T_0 of CEP in different pressures.

6. General discussion

All grown single crystals show behavior in agreement with the general phase diagram. In Figure 6.1 we see evolution from paramagnetism with metamagnetic transition to ferromagnetism. All results of modified CW law fits are summarized in Table 6.1. All values are similar to pure UCoAl, expect for higher effective moment in our single crystals.

Table 6.1: Resulting parameters of modified CW law fit for different concentrations of $UCo_{1-x}Ru_xAl$. Data for pure UCoAl are taken from [1]

	x = 0.01	x = 0.005	x = 0.0025	x = 0
$\chi_0 \left[10^{-9}\mathrm{m}^3 \cdot \mathrm{mol}^{-1}\right]$	9.75	6.96	6.88	8
θ_P [K]	34.9	31.6	33.3	33
$\mu_\mathrm{eff}\,[\mu_\mathrm{B}]$	1.83	1.87	1.83	1.6

The increase of the a cell parameter with increasing ruthenium concentration can lead to reduced overlap of $5f$ orbitals on neighboring uranium ions and $5f$-d hybridization. This would mean weaker interaction between magnetic moments, but stronger localization. In our case we can see that interaction does not seem weaker because of emergency of ferromagnetism. This means that the main driving mechanism is localization of uranium magnetic moments. Not only cell parameters effect properties, but also ruthenium which is not isoelectronic substitution and thus has some effect on electronic properties.

The position in phase diagram in Figure 3.4a) of each single crystal can be deduced from our present results. $UCo_{0.9975}Ru_{0.0025}Al$ is between disappearance of ferromagnetism and UCoAl in ambient pressure, because it exhibits only metamagnetic transition with the critical field smaller than for UCoAl. Coexistence of ferromagnetism and metamagnetic transition in $UCo_{0.995}Ru_{0.005}Al$ puts it between CEP and disappearance of ferromagnetism. $UCo_{0.99}Ru_{0.01}Al$ exhibits only ferromagnetic ordering and thus is clearly in ferromagnetic dome of the phase diagram.

$UCo_{0.995}Ru_{0.005}Al$ shows signs of coexistence of ferromagnetism and metamagnetic transition from magnetic and electrical resistivity measurements. There is no clear indication of transition from paramagnetism to ferromagnetism in the temperature dependence of electrical resistivity. No anomaly is observed and we observe T^2 behavior in low temperatures up to 4 K. This indicates ferromagnetic behavior in low temperatures. From further analysis we determined inflection point to be around 8.2 K, which is not connected with ferromagnetic ordering or any other anomaly. In Figure 6.2 we see difference in behavior of temperature dependence of electric resistivity between $UCo_{0.995}Ru_{0.005}Al$ and $UCo_{0.9975}Ru_{0.0025}Al$ mainly in low temperatures. $UCo_{0.9975}Ru_{0.0025}Al$ in low temperatures behaves like $T^{3/2}$, which is common power law in itinerant magnets above disappearance of ferromagnetism [22]. This agrees with disappearance of ferromagnetism in $UCo_{0.9975}Ru_{0.0025}Al$. Inflection point is found around 10.2 K, and it is not connected to any phenomenon, similarly to $UCo_{0.995}Ru_{0.005}Al$.

Metamagnetic transition is clearly visible in magnetoresistivity and the critical fields agree with critical fields determined from hysteresis loops for both single

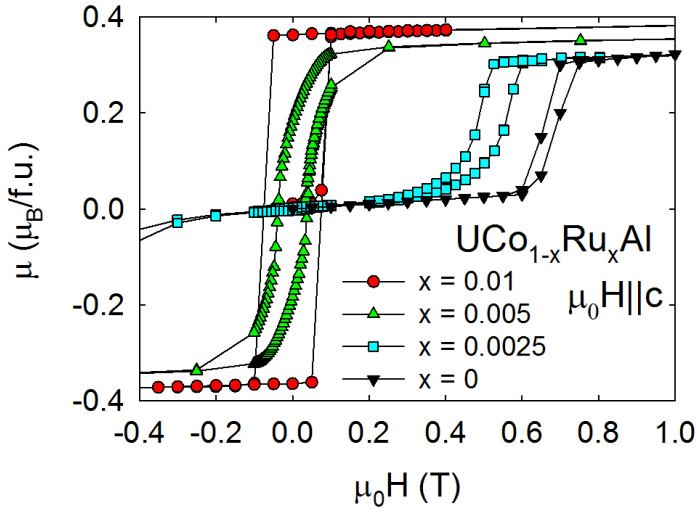

Figure 6.1: Hysteresis loops of $UCo_{1-x}Ru_xAl$ in 1.8 K for different composition. UCoAl data taken from [21].

crystals. Behavior below metamagnetic transition shows slow decrease with increasing magnetic field as in UCoAl [21]. The difference between temperature dependence of electric resistivity in zero magnetic field and 9 T magnetic field is plotted in Figure 6.3. This difference is connected with spin fluctuations, which also occur in pure UCoAl [32] and those spin fluctuations are connected to metamagnetic transition as mentioned in [31]. Spin fluctuation are stronger in $UCo_{0.9975}Ru_{0.0025}Al$ as the difference of the electric resistivity is higher compared to $UCo_{0.995}Ru_{0.005}Al$. This is probably due to the existence of a ferromagnetic ordering in $UCo_{0.995}Ru_{0.005}Al$, which suppresses spin fluctuations.

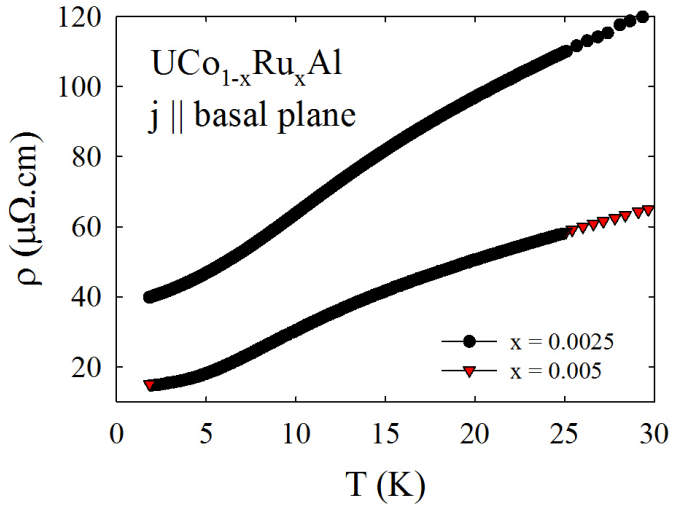

Figure 6.2: Temperature dependence of electrical resistivity of $UCo_{1-x}Ru_xAl$.

Pressure experiments showed clear wing structure for $UCo_{0.995}Ru_{0.005}Al$ and $UCo_{0.9975}Ru_{0.0025}Al$ similar to UCoAl and other quantum itinerant ferromagnets.

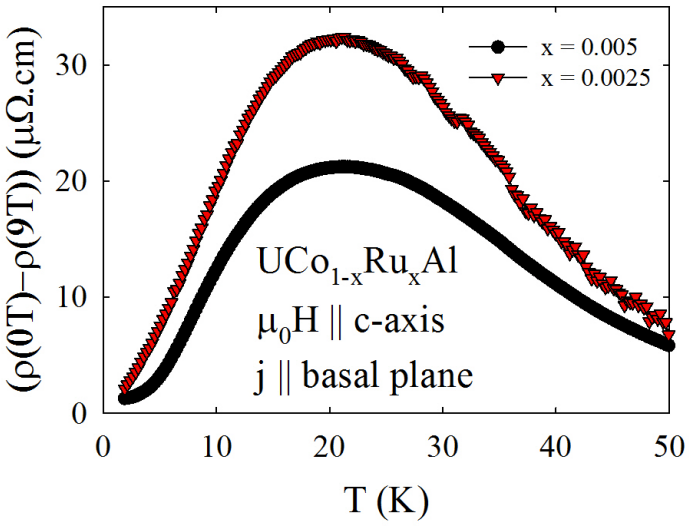

Figure 6.3: Temperature dependence of difference of the electrical resisitivity in zero and 9 T magnetic field for $UCo_{1-x}Ru_xAl$.

The temperature of CEP in ambient pressure was hard to determine thanks to either shape of the hysteresis loops or not enough data in different temperatures. This had effect on $UCo_{0.9975}Ru_{0.0025}Al$, where the temperature of CEP is 0.5 K lower than for UCoAl. Still we see very similar temperatures of CEP to CEP of UCoAl. We were not able to suppress CEP to QCEP, because of the limit of available pressure cells. Experiments in higher pressures are in preparations to map whole phase diagram and find QCEP.

Recent results on URhAl [24] and theoretical work [22] suggest existence of area in the general phase diagram, where ferromagnetism and metamagnetism coexist. Transition from paramagnetism to ferromagnetism in this area is called weak first order transition [22], meaning that latent heat is very small. Our results suggest that $UCo_{0.995}Ru_{0.005}Al$ exists in this part of the general phase diagram. Because the transition is weak, we were not able to observe it and other experiments are needed to confirm order of this transition.

Ferromagnetic ordering can also come from larger than expected clustering, where high concentration of Ru would be present in large volumes. Contrary to this there are other results similar to ours which show similar behavior like UCoAl doped by iron [33] or nonstochiometric UCoAl [34], which suggest this part of the general phase diagram is reachable and $UCo_{0.995}Ru_{0.005}Al$ is near it or in it. By doping we also introduce disorder, which has negative effect on the general phase diagram and in fact can destroy wing structure. From low residual resistivity of order $10^1 \mu\Omega \cdot$ cm in $UCo_{0.995}Ru_{0.005}Al$ and $UCo_{0.9975}Ru_{0.0025}Al$, we can say that our crystals have low disorder and high enough quality, which is needed to achieve phase diagram in Figure 3.4a). Lower quality would destroy wing structure and the phase diagrams would be similar to one in Figure 3.4b) or 3.4d). For our crystals wing structure is preserved and doping does not seem to have any effect on phase diagram from our present results.

7. Conclusions and future plans

We have grown single crystals of nominal compositions $UCo_{0.99}Ru_{0.01}Al$, $UCo_{0.995}Ru_{0.005}Al$ and $UCo_{0.9975}Ru_{0.0025}Al$. All single crystals crystallize in hexagonal ZrNiAl-type structure. We have done magnetic and electrical resistivity measurements in ambient pressures as functions of temperature and magnetic field and magnetic measurements in hydrostatic pressure as functions of magnetic field.

We observed transition from paramagnetic ground state with metamagnetic transition to low temperature ferromagnetism by increasing ruthenium concentration. Magnetic measurements and magnetoresistivity confirms existence of metamagnetic transition in $UCo_{0.995}Ru_{0.005}Al$ and $UCo_{0.9975}Ru_{0.0025}Al$, and with increasing ruthenium concentration critical field decreases. Ferromagnetism exists in $UCo_{0.99}Ru_{0.01}Al$ and $UCo_{0.995}Ru_{0.005}Al$ in ambient pressure. The temperature dependence of electric resistivity for $UCo_{0.995}Ru_{0.005}Al$ shows ferromagnetic behavior in low temperatures. Coexistence of ferromagnetism and metamagnetic transition in $UCo_{0.995}Ru_{0.005}Al$ implies that the transition from paramagnetism to ferromagnetism is of the first order and can be described as weak within context of proposed theory.

Wing structure of proposed phase diagram was found in $UCo_{0.995}Ru_{0.005}Al$ and $UCo_{0.9975}Ru_{0.0025}Al$ by magnetic measurements in hydrostatic pressure up to 1 GPa. Increase of the critical field and decrease of the temperature of CEP with increasing pressure was observed. In low pressure for $UCo_{0.995}Ru_{0.005}Al$ disappearance of ferromagnetism should be observable. In higher pressure existence of QCEP is expected.

Signs of existence of spin fluctuations in $UCo_{0.995}Ru_{0.005}Al$ and $UCo_{0.9975}Ru_{0.0025}Al$ were found in temperature dependence of electrical resistivity for different magnetic fields.

Our single crystals show very interesting physical properties, especially $UCo_{0.995}Ru_{0.005}Al$ and $UCo_{0.9975}Ru_{0.0025}Al$. Electric resistivity, Hall effect and dillatometry experiments in hydrostatic pressure on $UCo_{0.995}Ru_{0.005}Al$ are already prepared and same experiments will be done on $UCo_{0.9975}Ru_{0.0025}Al$. We will focus on low pressures to observe disappearance of ferromagnetism.

Author plans to continue working with uranium based compounds with similar phase diagram in his PhD thesis. Microscopical studies of spin fluctuations and origin of other phenomena can be done in ILL on THaLES spectometer.

References

[1] V. Sechovsky, L. Havela, F. R. de Boer, J. J. M. Franse, P. A. Veenhuizen, J. Sebek, J. Stehno, and A. V. Andreev. Systematics across the UTX series (T = Ru, Co, Ni; X = Al, Ga, Sn) of high-field and low-temperature properties of non-ferromagnetic compounds. *Physica B+C*, 142(3):283–293, 1986.

[2] D. Belitz, T. R. Kirkpatrick, and Jörg Rollbühler. Tricritical behavior in itinerant quantum ferromagnets. *Phys. Rev. Lett.*, 94:247205, Jun 2005.

[3] A. V. Andreev, L. Havela, V. Sechovsky, M. I. Bartashevich, J. Sebek, R. V. Dremov, and I. K. Kozlovskaya. Ferromagnetism in the $UCo_{1-x}Ru_xAl$ quasiternary intermetallics. *Philosophical Magazine B-Physics of Condensed Matter Statistical Mechanics Electronic Optical and Magnetic Properties*, 75(6):827–844, 1997.

[4] S. Blundell. *Magnetism in Condensed Matter*. Oxfor University Press, Grear, 2001.

[5] N. W. Ashcroft and N. D. Mermin. *Solid state physics*. Science: Physics. Saunders College, 1976.

[6] T. Kasuya. A theory of metallic ferro- and antiferromagnetism on zener's model. *Progress of Theoretical Physics*, 16(1):45–57, 1956.

[7] M. A. Ruderman and C. Kittel. Indirect exchange coupling of nuclear magnetic moments by conduction electrons. *Phys. Rev.*, 96:99–102, 1954.

[8] K. Yosida. Magnetic properties of Cu-Mn alloys. *Phys. Rev.*, 106:893–898, 1957.

[9] P. Fulde and M. Loewenhaupt. Magnetic excitations in crystal-field split 4f systems. *Adv. Phys.*, 34(5):589–661, 1985.

[10] V. Sechovsky and L. Havela. *Chapter 1 Magnetism of ternary intermetallic compounds of uranium*, volume Volume 11, pages 1–289. Elsevier, 1998.

[11] D. Belitz and T. R. Kirkpatrick. Quantum phase transitions. In J. Karkheck, editor, *Dynamics: Models and Kinetic Methods for Non-equilibrium Many Body Systems*, page 399, 2000.

[12] J. A. Hertz. Quantum critical phenomena. *Phys. Rev. B*, 14:1165–1184, Aug 1976.

[13] Masuo Suzuki. Relationship between d-dimensional quantal spin systems and (d+1)-dimensional ising systems: Equivalence, critical exponents and systematic approximants of the partition function and spin correlations. *Progress of Theoretical Physics*, 56(5):1454–1469, 1976.

[14] C. Kittel. *Introduction to solid state physics*. 1976.

[15] L. Havela. Magnetism and electronic structure of metallic systems. University Lecture, 2014.

[16] A. Huxley, E. Ressouche, B. Grenier, D. Aoki, J. Flouquet, and C. Pfleiderer. The co-existence of superconductivity and ferromagnetism in actinide compounds. *Journal of Physics-Condensed Matter*, 15(28):S1945–S1955, 2003.

[17] K. Prokeš, T. Tahara, Y. Echizen, T. Takabatake, T. Fujita, I.H. Hagmusa, J.C.P. Klaasse, E. Brück, F.R. de Boer, M. Diviš, and V. Sechovský. Electronic properties of a URhGe single crystal. *Physica B: Condensed Matter*, 311(3–4):220 – 232, 2002.

[18] N. T. Huy, A. Gasparini, D. E. de Nijs, Y. Huang, J. C. P. Klaasse, T. Gortenmulder, A. de Visser, A. Hamann, T. Görlach, and H. v. Löhneysen. Superconductivity on the border of weak itinerant ferromagnetism in UCoGe. *Phys. Rev. Lett.*, 99:067006, Aug 2007.

[19] A. Palacio-Morales, A. Pourret, G. Knebel, T. Combier, D. Aoki, H. Harima, and J. Flouquet. Metamagnetic transition in UCoAl probed by thermoelectric measurements. *Phys. Rev. Lett.*, 110:116404, Mar 2013.

[20] T. Goto, T. Sakakibara, K. Murata, H. Komatsu, and K. Fukamichi. Itinerant electron metamagnetism in YCo_2 and $LuCo_2$. *Journal of Magnetism and Magnetic Materials*, 90–91(0):700 – 702, 1990.

[21] Dai Aoki, Tristan Combier, Valentin Taufour, Tatsuma D. Matsuda, Georg Knebel, Hisashi Kotegawa, and Jacques Flouquet. Ferromagnetic quantum critical endpoint in UCoAl. *Journal of the Physical Society of Japan*, 80(9):094711, 2011.

[22] M. Brando, D. Belitz, F. M. Grosche, and T. R. Kirkpatrick. Metallic Quantum Ferromagnets. *ArXiv e-prints*, February 2015.

[23] V. Taufour, D. Aoki, G. Knebel, and J. Flouquet. Tricritical point and wing structure in the itinerant ferromagnet UGe_2. *Phys. Rev. Lett.*, 105:217201, Nov 2010.

[24] Yusei Shimizu, Daniel Braithwaite, Bernard Salce, Tristan Combier, Dai Aoki, Eduardo N. Hering, Scheilla M. Ramos, and Jacques Flouquet. Unusual strong spin-fluctuation effects around the critical pressure of the itinerant ising-type ferromagnet URhAl. *Phys. Rev. B*, 91:125115, Mar 2015.

[25] M. Uhlarz, C. Pfleiderer, and S. M. Hayden. Quantum phase transitions in the itinerant ferromagnet $ZrZn_2$. *Phys. Rev. Lett.*, 93:256404, Dec 2004.

[26] J. Rodriguez-Carvajal. Recent advances in magnetic structure determination by neutron powder diffraction. *Physica B: Condensed Matter*, 192(1-2):55 – 69, 1993.

[27] http://www.tescan.com/.

[28] http://www.qdusa.com/.

[29] http://lmnt.cz/instruments/cells.

[30] Alexander V. Andreev, Nikolai V. Mushnikov, Martin Diviš, Fuminori Honda, Vladimir Sechovský, and Tsuneaki Goto. Influence of isoelectronic substitutions on the magnetism of UCoAl. *Phys. Rev. B*, 71:094437, Mar 2005.

[31] T. D. Matsuda, H. Sugawara, Y. Aoki, H. Sato, A. V. Andreev, Y. Shiokawa, V. Sechovsky, and L. Havela. Transport properties of the anisotropic itinerant-electron metamagnet UCoAl. *Phys. Rev. B*, 62:13852–13855, Dec 2000.

[32] Jan Prokleška, Jana Vejpravová, and Vladimír Sechovský. Magnetoelastic effects in UCoAl. *Journal of Magnetism and Magnetic Materials*, 310(2, Part 2):1784 – 1785, 2007. Proceedings of the 17th International Conference on Magnetism The International Conference on Magnetism.

[33] N. V. Mushnikov, T. Goto, A. V. Andreev, H. Yamada, and V. Sechovsky. Physics of anisotropic itinerant 5f-electron metamagnetism in $UCo_{1-x}T_xAl$ (T=Fe, Ni). *Journal of Magnetism and Magnetic Materials*, 272-276, Supplement(0):E207–E213, 2004.

[34] A. V. Andreev, M. I. Bartashevich, T. Goto, K. Kamishima, L. Havela, and V. Sechovský. Effects of external pressure on the 5f-band metamagnetism in UCoAl. *Phys. Rev. B*, 55:5847–5850, Mar 1997.

List of Tables

5.1 Cell parameters for $UCo_{1-x}Ru_xAl$. Data for UCoAl were taken from [30]. 26
5.2 Critical fields and critical temperatures for $UCo_{0.995}Ru_{0.005}Al$ in different pressures. 33
5.3 Critical fields and critical temperatures for $UCo_{0.9975}Ru_{0.0025}Al$ in different pressures. 34

6.1 Resulting parameters of modified CW law fit for different concentrations of $UCo_{1-x}Ru_xAl$. Data for pure UCoAl are taken from [1] 36